The 2011 Cordón Caulle eruption triggered by slip on the Liquiñe-Ofqui fault system

C. Novoa [a,*], M. Gerbault [a], D. Remy [a], J. Cembrano [b,j], L.E. Lara [c,h], J. Ruz-Ginouves [b], A. Tassara [d,i], J.C. Baez [e], R. Hassani [f], S. Bonvalot [a], R. Contreras-Arratia [g]

[a] GET/UMR5563 (UPS, CNRS, IRD, CNES); Obs. Midi-Pyrénées, Université P. Sabatier, Toulouse, France
[b] Department of Structural and Geotechnical Engineering, Pontificia Universidad Católica de Chile, Santiago, Chile
[c] Servicio Nacional de Geología y Minería, Av. Santa María 0104, Santiago, Chile
[d] Departamento Ciencias de la Tierra, Facultad de Ciencias Químicas, Universidad de Concepción, Victor Lamas 1290, Concepcion, Chile
[e] Centro Sismológico Nacional, Universidad de Chile, Santiago, Chile
[f] Université Côte d'Azur, CNRS, Observatoire de la Côte d'Azur, IRD, Géoazur, 250 rue Albert Einstein, Sophia Antipolis 06560 Valbonne, France
[g] Seismic Research Centre, the University of the West Indies, St. Augustine, Trinidad and Tobago
[h] CIGIDEN (Research Centre for Integrated Risk Management), Chile
[i] Nucleo Milenio CYCLO: The Seismic Cycle along Subduction Zones, Chile
[j] Andean Geothermal Centre of Excellence (CEGA), Universidad de Chile, Santiago, Chile

ARTICLE INFO

ABSTRACT

Determining the mechanisms that promote large silicic eruptions is one of the biggest challenges in volcanic hazard assessment. The 2011-2012 Cordón-Caulle eruption in Chile was one of the largest silicic eruptions of the 21st century and was characterized by a rapid change from explosive to effusive behavior. This eruption was preceded by inflation from 2007 to 2009, followed by two years of barely any ground deformation. Despite intensive monitoring by geodetic and seismological data, its trigger remains undetermined. Here, we benefit from SAR imagery over the Puyehue Cordón-Caulle Volcanic Complex acquired by ALOS-1, ENVISAT and SENTINEL-1 data, to analyze the temporal and spatial behavior of ground displacements before, during and after the eruption. First, we find that a similar prolate spheroidal source explains the ground deformation for the pre-eruptive and post-eruptive periods. Then, we use 3D numerical elasto-plastic models to assess the failure conditions resulting from the pre-eruptive magma injection. Our results show that such a magma injection was too small to trigger the eruption. Therefore we explore other eruption triggers. Analytical elastic inversion models show that the ground displacements observed during the explosive phase may have been produced by slip motion along a NNW-striking dextral-strike slip, double-branch fault of the north-trending Liquiñe-Ofqui Fault System (LOFS), or along a single southern branch fault of the LOFS and collapse of the caldera. When investigating the elasto-plastic deformation pattern resulting from dextral slip along this branch-fault system, we obtain a sub-vertical dilatational plastic zone that connects the reservoir wall to the surface in a location that coincides with that of the 2011 eruption. Hence, we propose that this LOFS branch-fault eventually destabilized (perhaps weakened by the 2007-2009 episode of magma injection), and then slipped in a way that opened channels for fluid migration from the magma reservoir up to the surface.

© 2022 Elsevier B.V. All rights reserved.

1. Introduction

Silicic volcanoes produce the most explosive and hazardous eruptions in the world, covering large areas with ash and inducing potentially global climatic effects. Therefore, understanding the mechanisms that control explosive activity is one of the most im-portant topics in volcanic hazards forecasting. Many active silicic volcanoes are located in the Southern Volcanic Zone of Chile (SVZ), among which the Puyehue Cordón Caulle Volcanic Complex (PC-CVC) stands as one of the largest and most active.

The PCCVC is composed of three main structures trending NW to SE: the ~10 km wide Cordillera Nevada caldera to the northwest, the ca. 13 km long central Cordón Caulle fissure system, and the Puyehue stratovolcano to the south-east (Fig. 1). Volcanic activity started ca. 0.5 Ma with a wide range of compositions, evolving to mostly rhyodacitic and rhyolitic magmas in the Late Pleistocene-
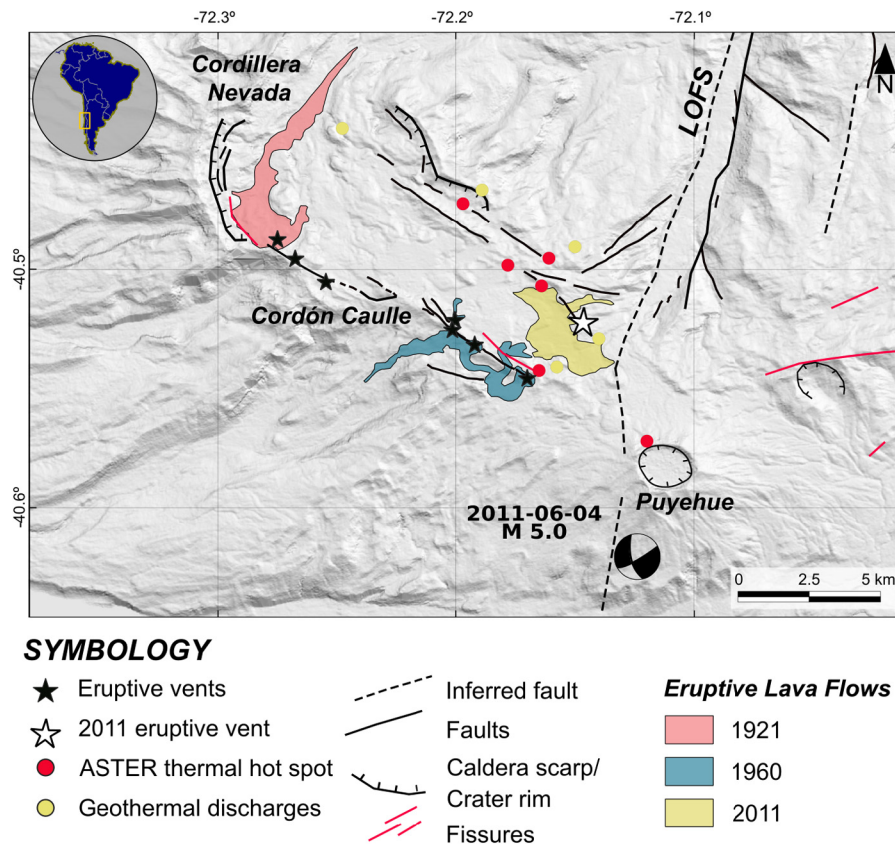
Fig. 1. The Cordón Caulle volcanic complex area (PCCVC), displaying fault traces and the last three eruptive vents. See appendix A for a regional map view of structures and seismicity in the SVZ.

Holocene for, both the Cordón Caulle fissure system and the Puyehue volcano (Lara et al., 2006; Singer et al., 2008). The last three eruptions (1921, 1960 and 2011) display similar magma compositions, indicating that they were fed by the same reservoir at depth (Jay et al., 2014). However, they occurred at different places along the volcanic complex. The 1921 vent was located close to the Cordillera Nevada Caldera while the two others occurred along the southern and northern flanks of the fissure system (Fig. 1).

The 2011 eruption at PCCVC was one of the largest sub-aerial eruptions of the 21st century. Despite intensive monitoring by geodetic and seismological data, its primary trigger remains an open issue (Jay et al., 2014; Wendt et al., 2017; Delgado, 2020). The eruption was preceded by an inflation of 22 cm/yr spanning the 2007-2009 period, followed by two years of barely any ground deformation. Jay et al. (2014) associated this inflation stage with the injection of 0.05 km^3 of mafic magma in a reservoir located at 4-9 km depth. Considering that this volume of intruded magma was too small to fail the bedrock and, that no direct sign of ascending magma was observed prior to the eruption, these authors concluded that this pre-eruptive inflation could not have triggered the 2011 eruption.

The 2011 eruption started on June 04 with an explosive phase of pyroclastic ejecta and gas-venting from a ∼10 km high column that lasted 7-9 days (Bonadonna et al., 2015), followed by lava effusion on June 12-13 until March 2012 (Bertin et al., 2015). During the explosive phase, a substantial interferometric signal was detected from an ENVISAT ascending interferogram encompassing the first three days of the eruption, which was interpreted as mainly due to subsidence (Jay et al., 2014; Wendt et al., 2017). These authors proposed that this subsidence (reaching about 80 cm) was induced by the volume decrease of about 0.11 km^3 of two magma bodies located beneath PCCVC at 4 and

6 km depth, respectively. Nevertheless, the inconsistency between this geodetic volume change at depth and the volume of erupted tephra (0.27 km^3 DRE) during the first three days of the eruption led Wendt et al. (2017) to propose an alternative hypothesis. They modeled part of the ground surface displacement as a closing dyke-like structure with an oblique left-lateral normal strike-slip motion along the graben. While this proposition provides interesting insights on a non-magmatic trigger of the eruption, the concept of a closing dyke structure remains problematic because although it allows the transport of magma to the vent, it fails to explain where the magma was extracted from.

The present paper performs a detailed investigation of the pre-existing tectonic structures at play during the pre-eruptive and the explosive phase of the 2011 eruption, associated with the observed InSAR LOS displacement. Combining analytical and finite-element modeling, we assess the mechanical state of the crust induced by the 2007-2009 magma injection, and then we test two hypotheses of eruption trigger by analyzing elastic and elasto-plastic strain-stress patterns in the host rock surrounding the magma reservoir.

2. The tectono-volcanic setting of PCCVC

In the Southern Andean Volcanic Zone, the N78°E oblique convergence between the Nazca and South-America plates promotes a regional transpressional regime with the maximum shortening axis trending N64°E (Cembrano and Lara, 2009; Pérez-Flores et al., 2016). Within the SVZ, the 1200 km long margin-parallel Liquiñe-Ofqui Fault System (LOFS) extends north-south between 36 and 46°S as a dextral strike-slip fault, accommodating at present 1 to 7 mm/yr of the ca. 70 mm/yr of plate convergence (e.g. Stanton-Yonge et al., 2016). Large stratovolcanoes are elongated in the NE-SW direction, but some also lie along NW-trending directions (Lara et al., 2006; Cembrano and Lara, 2009; Sielfeld et al., 2019).
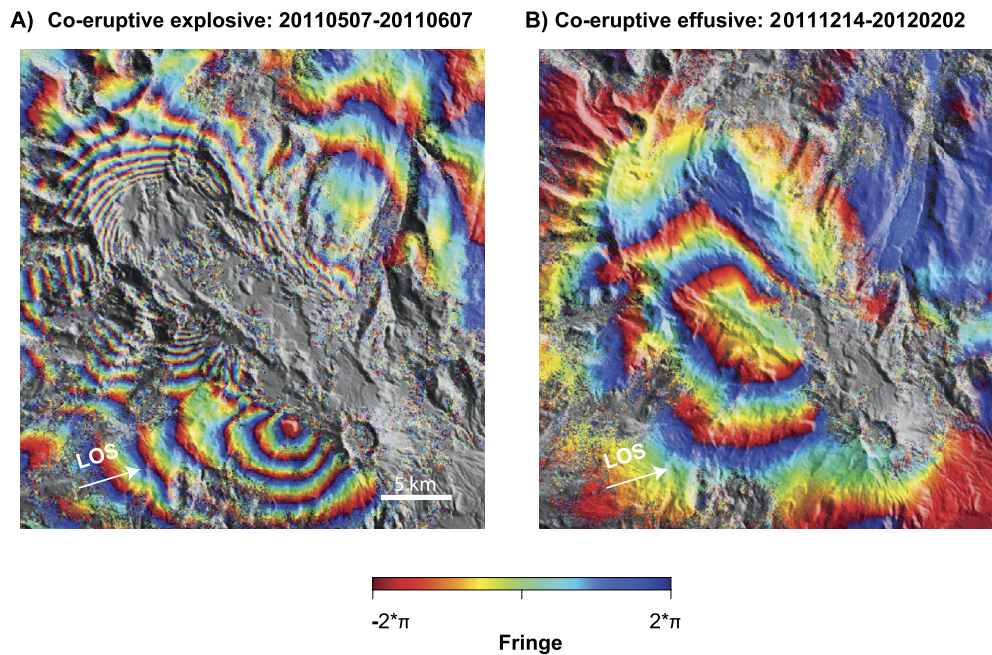
A) Co-eruptive explosive: 20110507-20110607   B) Co-eruptive effusive: 20111214-20120202

Fig. 2. Subset of unwrapped interferograms overlaid onto a shaded relief map. A) Ascending ENVISAT encompassing the explosive eruption occurred at the beginning of June 2011, for 7-9 days. B) Ascending ENVISAT interferogram encompassing the effusive period of the eruption, from June 12-13 to March 2012. The satellite to ground radar line of sight (LOS) is shown with a black arrow. LOS displacements toward the satellite are positive (i.e., slant range decrease). Areas in grey correspond to low coherence areas or to areas characterized by unwrapping errors. Coordinates are expressed in UTM-WGS84 (18 zone South).

Small monogenetic eruptive centers in turn are located along the master fault of the LOFS. It has long been suggested that the NE-trending volcanic alignments correspond to transtensional domains associated with the dextral transpressional setting of the arc. In contrast, the NW-oriented volcanic complexes appear controlled by NW transverse pre-Andean fault systems (López Escobar et al., 1995; Cembrano and Lara, 2009). Several studies have argued that during interseismic periods, deformation is partitioned in the arc and forearc domains, with the activation of N-S trending dextral strike-slip faulting, coeval with extension along NE-striking structures and sinistral-reverse displacement along NW-striking inherited structures (Pérez-Flores et al., 2016; Sielfeld et al., 2019; Lupi et al., 2020).

The Puyehue Cordón Caulle Volcanic Complex (PCCVC, Fig. 1) is one of those volcanic centers lying on top of a basement NW-trending structure, and like others it is characterized by a wide variety of magma compositions including felsic volcanism, as opposed to dominantly mafic volcanism along NE-trending domains. López Escobar et al. (1995) proposed that the felsic compositions result from the NW-trending domains being compressional in nature since they strike nearly orthogonal to the interseismic shortening direction, hereby favoring long-term intra-crustal residence of magma. The Cordón Caulle geothermal area is located inside a depression that forms a 13 km × 6 km, NW-SE elongated volcano-tectonic corridor hosting numerous monogenetic centers and hot-springs, most of which stand along its edges (Sepúlveda et al., 2005, Fig. 1). NE-trending gravimetric profiles across this depression yield a residual negative anomaly reaching about 20 mGal at its center, attributed by Sepúlveda et al. (2005) to the presence of an infill formed by dacite–rhyolite lavas and tephra in the first ~600 m depth, and which is bordered by inward dipping normal-like fault zones. Kilometers away where lava cover disappears, exposures of granitic rocks from the crystalline basement are mostly observed (Lavenu and Cembrano, 1999). Here, as a first hypothesis for the 2011 eruption trigger, we shall consider the influence of this NW-oriented caldera-graben structure by considering a mechanically weaker domain.

As a second hypothesis for the eruption trigger, we shall consider the influence of a dextral-slip motion of the LOFS or of one of its numerous branching faults, in consistency with mapped meso-scale brittle faults and seismological data. On the day of the 2011 eruption, the USGS Catalog reported 22 earthquakes of Mw between 3.6 to 5 and depths between 3 and 20 km. The focal mechanism of the largest Mw 5.0 event was reported by the GCMT project, with a dextral-strike slip motion nodal plane consistent with the LOFS kinematics (Appendix A), and located about 5 km away from the volcanic complex. We note that a similar focal mechanism was recorded in 1999 for a Mw 5.4 event at 15 km depth (Cembrano and Lara, 2009) as well as another one in 2010 for a Mw 5.1 event about 90 km further north (CMT Catalog, Fig. A.1). Our own moment tensor inversion of this event confirms a dextral strike-slip motion, and re-estimates its location on the fault trace at 7 km depth (Appendix A). Additionally, satellite images show that the earliest activity of the 2011 explosive eruption was sourced from two cones aligned N18°W (Schipper et al., 2013). This N18°W strike happens to be very close to the N20°W strike of the second nodal plane of the Mw 5.0 seismic event.

3. InSAR DATA and processing

The SAR images covering the different periods of activity at PCCVC were acquired by three satellite missions: L-band Stripmap mode images from ALOS-1 operated by the Japan Aerospace Exploration Agency (JAXA), C-band ENVISAT ASAR Image Mode data and C-band Interferometric Wide Swath mode images Sentinel-1A/B, both from the European Space Agency. All treatment details of the InSAR images are explained in Appendix B.

4. Determining the geometry of the magmatic reservoir

In a first step we search for the geometry and location of a reliable active source able to explain the surface displacements observed during the complete eruptive cycle. Figs. 2, 3A and B show
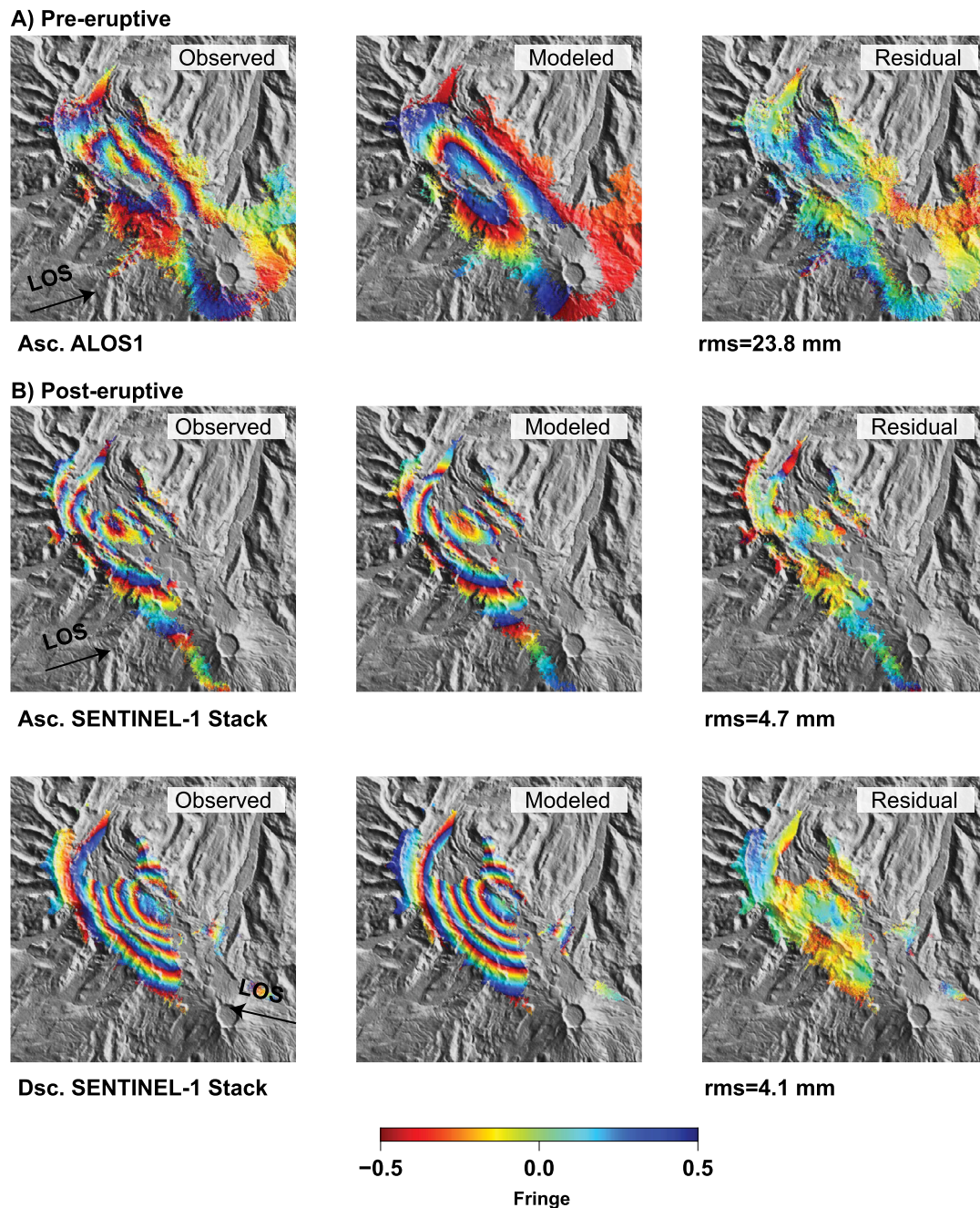
Fig. 3. Wrapped InSAR interferograms and inversion results for a prolate-spheroidal reservoir. Observed, modeled and residual ground displacements, for comparison between pre- and post-eruptive periods. Up) ALOS1 interferograms scene pairs 07 January 2007 to 10 January 2008. Middle) Stack of three ascending Sentinel-1 interferograms during the post-eruptive period. Bottom) Stack of four descending Sentinel-1 interferograms during the post-eruptive period. Each fringe (full color cycle) represents 2.83 cm (ASAR) or 11.81 cm (PALSAR) of range of change between the ground and the satellite. Areas that lack interferometric coherence are uncolored. Interferometric phase images are shown superimposed on the shaded-relief image. (For interpretation of the colors in the figure(s), the reader is referred to the web version of this article.)

the characteristic patterns of ground displacements observed by InSAR data at PCCVC during the co-eruptive, pre-eruptive and post-eruptive periods. The interferogram of the co-eruptive explosive phase covers the first 3 days of the eruption. The ground displacement pattern during this period is characterized by two lobes of slant range increase (ground moving away from satellite), one of ∼ 80 cm located within the Cordillera Nevada Caldera in the northwestern part of the graben, and the other one of ∼30 cm located in the southeastern part of the graben closer to the eruptive vent (Fig. 2A). A lobe of slant range decrease of ∼12 cm is also observed to the north-east of the volcanic complex. In contrast, during the co-eruptive effusive phase of the eruption from

July 2011 to February 2012, the pattern of ground displacements shows a unique lobe of slant range increase that is consistently oriented NW-SE, centered on the central part of the graben and close to the eruptive vent (Fig. 2B, the interferogram covers December 2011 to February 2012).

A similar NW-SE oriented pattern of slant range decrease is clearly identified by visual inspection of the pre-eruptive ALOS-1 and the post-eruptive Sentinel-1 interferograms (Fig. 3A-B). Both these interferograms have approximately the same LOS unit look vectors [−0.6049, −0.1966, 0.7716] and [−0.6113, −0.2093, 0.7660]. This similar pattern suggests that a similar physical process drove them, leading us to search for a single source geometry

able to explain both pre- and the post-eruptive observed ground displacements.

We use two stacks of three ascending and four descending Sentinel-1 interferograms, and two ALOS1 interferograms to search for the best geometry able to explain ground displacement at PC-CVC (the earliest and the latest images used in the stack are indicated in Table B.1). We assume an uncorrelated uncertainty of 1 and 1.5 cm for Sentinel-1 and ALOS1 data, respectively leading to uncertainties of 6 and 5 mm for the ascending and descending stacks, respectively.

We consider three different sources, including a spherical source (Mogi, 1958), a prolate spheroid (Yang et al., 1988) and an Okada-type dislocation (Okada, 1992) embedded in a homogeneous isotropic elastic half-space. Poisson's ratio $\nu = 0.25$ was assumed as well as a flat topography, considering that topographic slopes affected by the signal are less than the $10°$ limit for which their effects become significant (Cayol and Cornet, 1998). The model fitness is quantified using the weighted root-mean square of the residual phase (rms). We use a quadtree algorithm to subsample the data points, and a Levenberg-Marquardt algorithm to minimize the residuals. In agreement with previous studies (Wendt et al., 2017; Delgado, 2020) the best model is a prolate spheroidal reservoir yielding an rms of 4.1, 4.7 and 23.8 mm for the descending and ascending Sentinel-1 stacks, and for ALOS1 data, respectively (Table 1). The source was also inverted using the ascending and descending stacks of Sentinel-1 data conjointly, and yields only a slight increase of the resulting rms. Therefore a prolate spheroidal source appears a reasonable model to explain pre and post-eruptive surface displacements, acknowledging that the real medium is certainly more complex than in our models.

Next, we investigate parameters uncertainties for this best-fit model using a Monte-Carlo simulation. We first estimate the correlated noise from small temporal Sentinel-1 and ALOS-1 interferograms, and we approximate the InSAR noise using an exponential-type random noise of variance $0.8.10^{-4}$ m^2 and of correlation length 5 km. Next, we invert 200 independent trials with added correlated noise to the data, in order to estimate the confidence interval shown in Table 1. ALOS-1 data inversions favor a source located a little further to the west and striking a little further to the south compared to Sentinel-1 data inversions. Despite these differences, other parameters range close to each other. We conclude that the observed inflation during the pre- and post-eruptive periods were driven by a similar displacement source, best modeled by a prolate-spheroidal reservoir located at 4.5 km depth, elongated in the $130°$ direction (N40°W) and with major and minor axes of about 8 km and ~0.9 km (Fig. 3 and Table 1). With this geometry, the recorded InSAR pre-eruptive inflation is explained by a pressure increase (ΔP) of 32 MPa, given a bedrock shear modulus (G) of 20 GPa.

5. Mechanical state associated with the pre-eruptive inflation stage

In order to investigate the pre-eruptive conditions for rock mass failure around the inflating magma reservoir, we use the finite-element code *Adeli* (details below) to explore stress and deformation patterns resulting from an overpressure applied at the walls of the prolate-spheroidal source determined in section 4. Below, we first describe the predicted patterns of stress and deformation assuming elastic behavior in a homogeneous domain, then in a heterogeneous domain containing a relatively weak caldera-graben structure. Second, elasto-plastic rheology is considered to better track strain localization in the overlying crust where stresses exceed a failure threshold, for both shear and tensile failure modes. Accounting for this rheology allows to infer potentially fractures around the reservoir and their propagation throughout the bedrock

Table 1
Best fitting prolate spheroidal sources parameters. Latitude and longitude are expressed in km (UTM WGS84 zone 18 South).

Parameters	DSC STACK	95% CI	ASC STACK	95% CI	ASC ALOS1	95% CI	DSC STACK-ASC STACK	95% CI
Longitude (km)	736.332	(735.745;736.912)	737.680	(736.136;738.796)	737.724	(736.713;738.840)	736.598	(736.082;736.927)
Latitude km	5514.636	(5514.151;5515.037)	5513.531	(5512.537;5514.326)	5509.915	(5508.057;5511.366)	5514.244	(5513.952;5514.781)
Depth (km)	4.965	(4.530; 5.379)	4.526	(3.582;5.185)	3.666	(3.056;4.683)	4.512	(4.326;4.99)
Length (km)	7.600	(6.643;8.465)	9.474	(7.866;11.000)	10.395	(8.3168;12.6156)	7.768	(6.891;8.29)
Dip (°)	−2.5	(−9.2;5.7)	17.5	(10.6;20.0)	12.3	(10.2;16.3)	6.9	(−2.3;10.5)
Strike (°)	126.9	(119.8;135.3)	126.1	(120.9;134.5)	142.3	(138.4;148.0)	129.1	(121.0;135.2)
RMS (mm)	4.1		4.7		23.8		6.1	

upon loading, they may constitute pathways for magmatic fluids towards the surface.

5.1. Numerical method, assumptions and setup

The three-dimensional finite-element code *Adeli* uses the dynamic relaxation method (Cundall, 1989) to resolve the quasi-static equation of motion and determine stress and strain fields in elastic and elasto-plastic media. This time-explicit method uses an adaptative time-step together with damping of out-of-balance forces. It has been used for more than 30 yr in the engineering (*FLAC* code from *Itasca Consulting Group*) and Earth sciences communities, hence implementation details can be found in numerous places (Hassani et al., 1997; Cerpa et al., 2015; Gerbault et al., 2018; Novoa et al., 2019; Ruz-Ginouves et al., 2021). The finite-element mesh is first built using the *GMSH* mesher (illustrations and reference in Appendix C). Upon progressive loading, the initially elastic medium starts to yield plastically when the yield stress envelope for either Drucker-Prager shear failure (F_{DP}) or tensile failure (F_T) is reached:

$$F_{DP}(\sigma) = J_2(\sigma) + \frac{6sin(\phi)}{3 - sin(\phi)}I_1(\sigma) - \frac{6Ccos(\phi)}{3 - sin(\phi)} = 0, \qquad (1)$$

$$F_T(\sigma) = I_1(\sigma) - T = 0,$$

where ϕ is the friction angle, C is cohesion, T tensile strength. $I_1(\sigma) = \frac{1}{3}tr(\sigma)$ and $J_2(\sigma) = \frac{3/2\ (s:s)^{1/2}}{\sqrt{2}}$ are first and second invariants of the stress tensor σ ($s = \sigma - I_1(\sigma)$). Below we also display the strain invariants $I_1(\varepsilon)$, $J_2(\varepsilon)$, which derive similarly from the strain tensor ε. Sign convention is that positive $I_1(\sigma)$ or $I_1(\varepsilon)$ describes expansion. Plastic deformation is then determined with an associative flow rule for tensile failure and a non-associative flow rule for shear failure (here dilatancy is set to zero, cf. Ruz-Ginouves et al., 2021).

All simulations presented below were made assuming zero-friction angle and zero gravity, in order to reproduce the minimal conditions for plastic failure. This simulates effective properties of weakened crustal domains due to a variety of processes such as lithostatic pore-fluid pressure and recurrent micro-fracturing (Sibson, 2003; Suppe, 2014), a reasonable assumption considering that the PCCVC is one of the most active geothermal systems of the SVZ. Nevertheless, the reader can find in Appendix D complementary simulations assuming gravity and a friction angle of 30°, which represents dry and resistant crust failing at maximal pressure-load conditions.

Rewriting Eqs. (1) for zero-friction angle and zero gravity leads to shear failure initiating when $J_2(\sigma)=2C$ and tensile failure initiating when $I_1(\sigma)=T$. Cohesion and tensile strengths are chosen proportional to the shear modulus (e.g. Schultz, 1996), with a proportionality factor of 10^{-4} equal to that assumed by Zhan et al. (2019) for the Laguna del Maule Volcanic Complex, also located in the SVZ. For instance, a Young's modulus $E = 50$ GPa (corresponding to a shear modulus $G = 20$ GPa), provides $C = 25$ MPa and $T = 5$ MPa. With exact values being impossible to assess in the area, we assume a range of values $E = 12.5 - 50$ GPa, $C = 5 - 25$ MPa and $T = 1 - 5$ MPa, compatible with common estimates (Heap et al., 2020).

5.2. Stress and strain patterns assuming an elastic bedrock

First we simulate an overpressurized cavity embedded in a homogeneous elastic medium (mesh shown in Appendix C.1). The observed ∼40 cm of LOS surface displacements during the pre-eruptive period can be explained by an overpressurized source (ΔP) of 8 MPa or 32 MPa, given a shear modulus of either 5 GPa

or 20 GPa, respectively. Both options produce the same pattern of dilatation, with maximums at the tips of the spheroid's major axis and constriction at its roof (Figs. 4A-B). These areas of maximum dilatation can be associated with the opening of micro-fractures promoting seismicity (Simpson et al., 2001; Lamur et al., 2017), and may explain the seismicity reported in the Cordillera Nevada during the pre-eruptive period (Wendt et al., 2017). In turn, the constrictional zone at the reservoir's roof tends to close the pore-space and impede fluid flow between the reservoir and the surface (as suggested by Gerbault et al., 2018; Zhan et al., 2019).

Second, we simulate the caldera-graben system at PCCVC (mesh shown in Appendix C.2), by inserting a weaker domain around the spheroidal reservoir, of shear modulus $G = 5$ GPa and embedded in a stiff bedrock of $G = 20$ GPa. An applied overpressure of 8 MPa (fitting surface displacements), produces dilatational areas mostly identical to the homogeneous case. However, constriction is intensified inside the compliant caldera-graben domain (Fig. 4C, Fig. 4D).

5.3. Elasto-plastic deformation

Then, we explore how bedrock failure might have been at play during the pre-eruptive inflation period in both these homogeneous and heterogeneous configurations. *Adeli* models with the failure parameters given above (section 5.1) show that the application of a reservoir overpressure $\Delta P = 32$ MPa provides first and second stress invariants maxima $I_1(\sigma)_{max} = 13$ MPa at the tips of the major axis, and $J_2(\sigma)_{max} = 55$ MPa around the minor axes (Fig. 5A-B-C-D). Hence, tensile failure expands outwards from the major-axis tips if bedrock tensile strength $T < 13$ MPa, while shear failure concentrates along the central minor axis if cohesion $C < 27.5$ MPa (Fig. 5E-F-G). Note that these plastic domains are restricted around the reservoir walls, far from the top surface, which illustrates why the pre-eruptive inflation was too small to promote an eruption. When we include a weak caldera-graben domain (e.g. the heterogeneous configuration), similar restricted deformation patterns are produced, leading to the same conclusion (Fig. 5H-I). Numerical simulations show that the reservoir overpressure would need to be doubled in both configurations for plastic domains to expand and connect the reservoir and the surface (this stage may be assimilated to the onset of an eruption, e.g. Gerbault et al., 2018). Furthermore, this connection to the surface occurs near the Cordillera Nevada, much further to the NW than the actual location of the 2011 eruptive vent (cf. Appendix D). Thus in either configurations our numerical simulations show that the pre-eruptive inflation could not have promoted the eruption. The resulting potential damage zones remain constrained close to the reservoir walls and never approach the location of the 2011 eruption. These results combined with the fact that no inflation was observed at the PCCVC's surface during the two years prior to the eruption, lead us to eliminate a magmatic inflow trigger.

6. Kinematic models of a tectonic trigger to the co-eruptive explosive phase

We explore now the possibility that slip along one of the tectonic structures identified in the area may have triggered the 2011 eruption. As a preliminary step, we need to subtract how much of the observed slant range increase associated with the explosive phase of the eruption could be attributed to the reservoir's emptying at depth. Therefore we estimate the volume change (DV) of the prolate reservoir during the explosive phase using (Mastin et al., 2008):
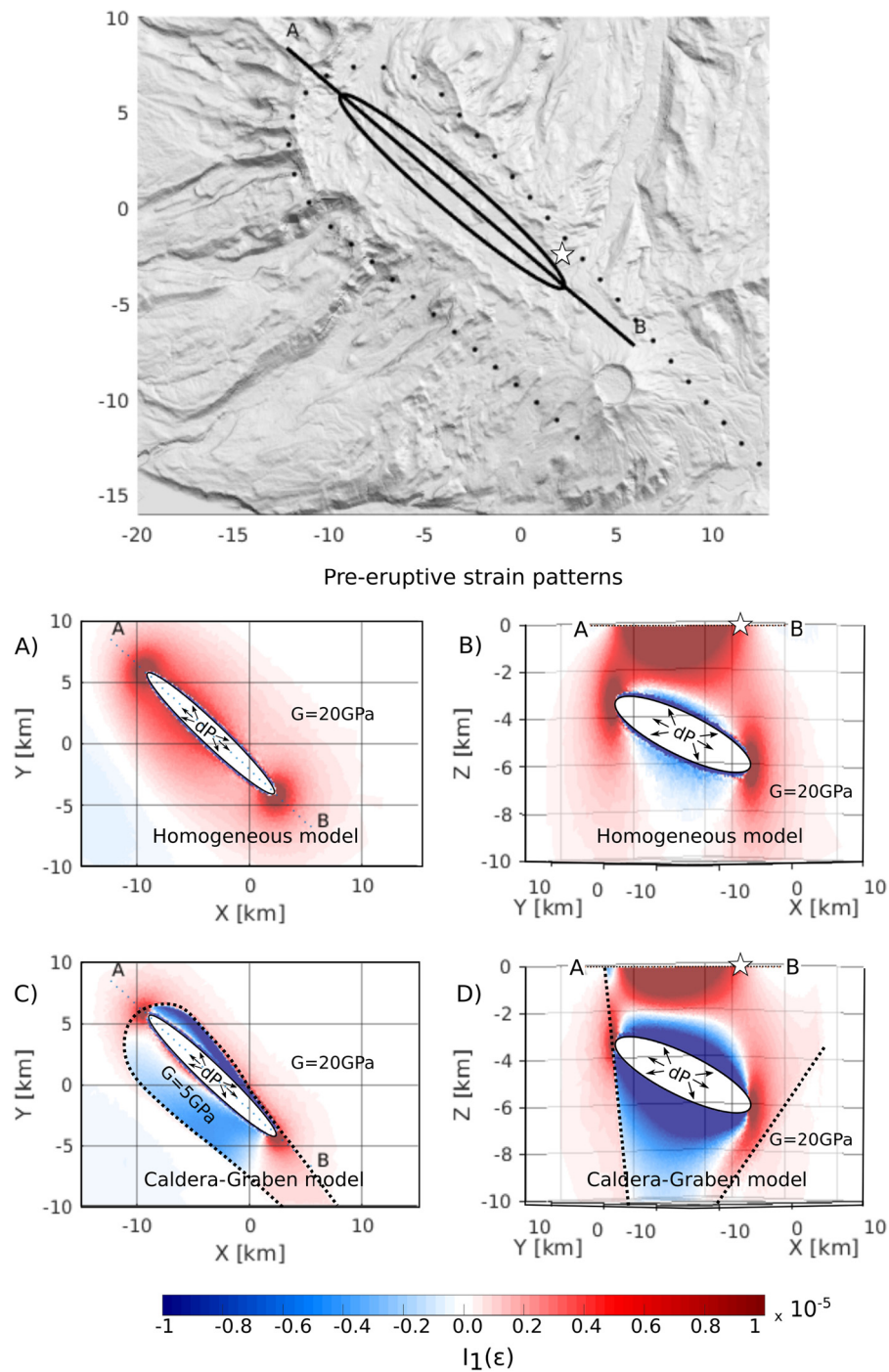
$$\frac{V_e}{DV} = -(1 + \frac{K_m}{K_r}) \qquad (2)$$

Fig. 4. Computed first invariant of the strain ($I_1(\varepsilon)$) with *Adeli*, for an overpressurized prolate-spheroidal cavity that best fits the pre-eruptive surface displacements in two configurations. A-B: the cavity is embedded in a homogeneous elastic medium with shear modulus $G = 20$ GPa. C-D: the cavity is surrounded by a weak caldera-graben domain with $G = 5$ GPa embedded in a medium with $G = 20$ GPa. Areas of dilatation (positive $I_1(\varepsilon)$) shown in red. A-C) Sub-horizontal plane view following the inclined major axis of the cavity, B-D) Vertical cross section following profile AB parallel to the cavity's major axis.
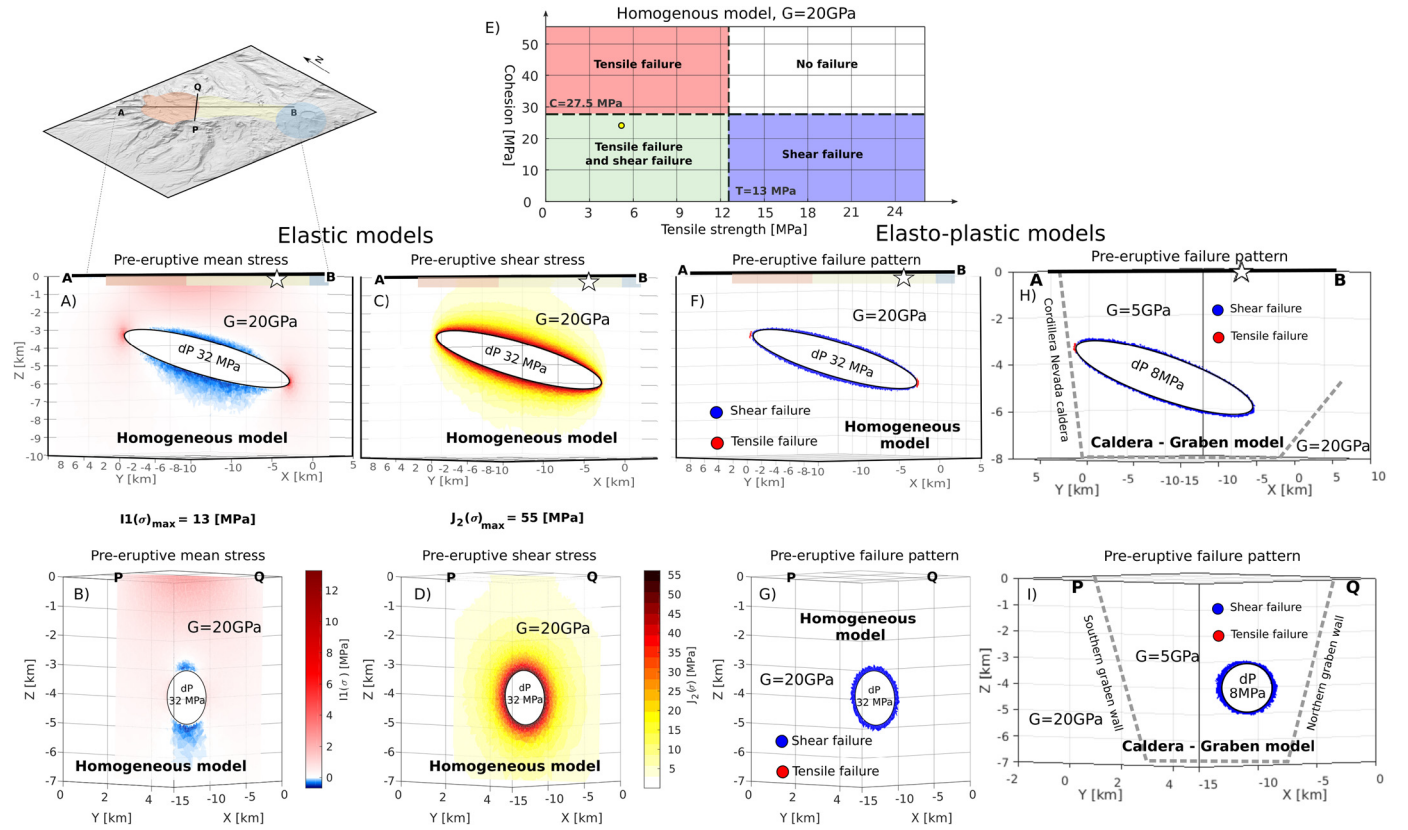
Fig. 5. Stress and strain patterns computed with *Adeli* throughout an homogeneous elastic bedrock of shear modulus $G = 20$ GPa and submitted to a (pre-eruptive) overpressure ΔP at the walls of a prolate-spheroidal reservoir, for elastic (A-B-C-D) and elasto-plastic (F-G) media. Two vertical cross sections are displayed: AB and OP. A-B) First stress invariant when $\Delta P = 32$ MPa: maximum $I_1(\sigma)$=13 MPa occurs at the tips of the reservoir, where tensile failure is expected. C-D) The second stress invariant concentrates along the minor axis of the reservoir. E) Predicted modes of failure in the elasto-plastic domain depending on tensile strength (T) and cohesion (C). The yellow circle locates the failure mode when $T = 5$ MPa and C=25 MPa (friction=0° and no gravity), illustrated below. F-G) The predicted patterns of failure satisfy Eqs. (1): tensile failure represented by red regions occurs at the tips of the major axis where $I_1(\sigma) > 5$ MPa. Shear failure represented by blue regions occurs elsewhere around the reservoir where $J_2(\sigma) > 50$ MPa. H-I) Shear and tensile failure patterns for an overpressurized reservoir embedded in weak caldera-graben structure with G=5 GPa in contrast to the rest of the bedrock where $G = 20$ GPa, when $\Delta P = 8$ MPa.

Taking into account the erupted volume (V_e), estimated by Pistolesi et al. (2015), the compressibility of the bedrock (K_r) and the magma (K_m) inferred by Wendt et al. (2017) and Jay et al. (2014), respectively, the volume change associated with this deep source must have been of the order of 0.03 km³. This volume change can only account for about 20% of the subsidence observed during the first 3 days of the eruption, supporting the argument that the other 80% of cumulated InSAR displacements must have a non-magmatic origin.

Next, we search for the best location and geometry of fault planes characterizing nearby tectonic structures. Two disconnected faults structures are identified and are each subdivided into multiple dislocation patches. To best fit the observed InSAR displacement resulting from slip along these patches, we compute ground surface displacements using the inversion algorithm provided by the Principal Component Analysis-based Inversion Method (PCAIM) software, which uses Okada's equations as Green's functions throughout an elastic medium (Kositsky and Avouac, 2010; Perfettini et al., 2010) technical details in Appendix E). In the following, the corresponding geodetic moments are also estimated, assuming $G = 20$ GPa in the bedrock.

6.1. Testing slip motion along the Caldera-Graben structure

As a first hypothesis, we investigate if a combination of downdip slip along the Cordillera Nevada and reverse-sinistral slip along the graben walls (consistent with the structural data mentioned in Section 2) can explain the remaining subsidence

observed during the explosive phase. We use the fault system geometry defined in section 5.2 and discretize it into 902 elementary patches 1.1×1.4 km² in size. In the PCAIM inversion, we constrain the rake angle and direction to normal in the Cordillera Nevada caldera, and to reverse-sinistral slip along the graben walls. In the end we could not obtain a satisfactory model fitting the InSAR data with this geometry, because we always need to extend the limit of the northern wall of the graben much further to the south-east than actually mapped (segment C-D in Fig. 6.A). This leads us to discard this hypothesis.

6.2. Testing slip motion along a branch fault of the LOFS

As a second hypothesis, we assess if the LOS displacement during the explosive phase of the eruption could be related to the activation of a branch of the LOFS. Therefore, we take the most north-south oriented plane deduced from the Mw 5.0 focal mechanism, whose location coincides with a fault trace inferred by the OVDAS (Appendix A). This nodal plane resembles the main trace of the LOFS, which is generally described as a subvertical fault zone (e.g., Sielfeld et al., 2019; Díaz et al., 2020). We use this assumption considering that at the scale of the PCCVC, the LOFS cannot be recognized from geomorphological features nor from the geophysical record. It is however supported by the N-S alignment of minor eruptive centers south of Puyehue volcano (Lara et al., 2006), an orientation that is also observed in other segments along the SVZ and that is thought to serve as pathways for primary basalts along the arc (Cembrano and Lara, 2009; McGee et al., 2017). There is

Fig. 6. InSAR best fit models for the interferogram shown Fig. 2A after removing the subsidence pattern caused by a volume change of ~0.03 km3 of the prolate spheroidal reservoir (left displays the modeled data, right displays its residual with observations). A) Caldera-Graben structure model. Black Line shows the geometry of the structure. Pure normal slip is imposed on the caldera border fault and reverse sinistral slip is imposed on the graben faults. B) Activation of a branch fault of the LOFS, along with a dextral-strike slip is imposed. Black Line shows the trace of the fault. This model explains 86% of the observed variance (rms 0.05 m). C) Caldera collapse and activation of the southern branch-fault only. The black rectangle represents the Okada-fault zone and the black line shows the location of the Caldera-border fault. This model explains 92% of the observed variance (rms 0.042 m).

also evidence of a near-vertical NS-trending fault from the geological record (Cembrano et al., 1996; Lavenu and Cembrano, 1999), where deformed rocks are now exhumed and eroded by glaciers shaping a large-scale fault system. The resulting fault zone is discretized into 638 elementary patches 1.2×1.4 km^2 in size, for inversion with PCAIM based on InSAR data. The best fitting model displays two slipping patches leading to a variance reduction of 86% and a rms = 0.05 m (Fig. 6B). This model fits InSAR data reasonably well, but systematic residuals remain visible near the fault trace. The biggest slipping patch is located to the north east of the graben, with a length of 15 km and a width of 7 km, while the smaller one is located to the south of the graben with a length of 7 km and a width of 6 km (Fig. 6B). These northern and southern slip patches each imply a geodetic moment of about 2.4×10^{18} N · m and 6.1×10^{17} N · m, respectively (discussed in section 7).

6.3. Slip motion along the southern branch-fault of the LOFS and Caldera collapse

The two hypotheses above lead us to propose a third scenario, which assesses the possibility that the LOS displacements were caused by a collapse of the Cordillera Nevada and concomitant slip motion along the southern branch-fault of the LOFS. Inversions of the LOS displacement in the vicinity of the caldera (section 6.1) combined with the Okada-model constrained by the CMT focal mechanism along the southern-branch fault (section 6.2), provides a best fitting model explaining 92% of the variance with a rms of 0.042 m. The patch located on the wall of the Cordillera Nevada Caldera provides a mean amount of slip of about 1.25 m onto a ∼10 km-deep and ∼15 km-long fault surface (Fig. 6C). The geodetic moments associated with these two slipping patches yield 3.77×10^{18} N · m and 2.23×10^{17} N · m, respectively.

7. Discussion

7.1. Geometry of the magmatic reservoir at PCCVC

The inversion of both pre- and post-eruptive InSAR ground displacements suggests that deformation was driven by inflation of a source of similar shape. Nevertheless, this similarity in shape remains difficult to link with the pattern of InSAR ground displacement during the effusive phase, which has been interpreted as mainly resulting from the emptying reservoir (Delgado, 2020; Fig. 2B). This explains why the temporal and spatial patterns of ground displacement had previously been interpreted with magma injection sources at different and independent locations, for the pre- and post-eruptive periods (Jay et al., 2014; Wendt et al., 2017; Delgado, 2020). While these interpretations offer the possibility to explain the ground displacements during the different phases of the volcanic cycle, they fail in providing a consistent framework for the evolution of the shallow magma plumbing system. The striking difference in pattern of ground displacement between the effusive phase and the pre- and post-eruptive phases suggests that it could have resulted from damaging of the shallow magma plumbing system and/or of the overlying hydrothermal system.

7.2. Kinematic models for the explosive phase of the eruption

Whereas 20% of the InSAR-observed subsidence is explained by 0.03 km^3 of decreasing volume of the magma reservoir, the remaining 80% can be accounted for by a kinematic model of motion along a branch-fault of the LOFS, accompanied or not by the collapse of the caldera (Figs. 6B-C). While the former model fits data slightly better (rms of 0.042 vs. 0.05 m), differences are small. In both solutions, systematic localized residuals are visible probably

because of the simplified assumptions of the structures geometry and rheology. These two models yield a geodetic moment release during the explosive phase of the eruption of 3.01×10^{18} and 3.99×10^{18} N·m, respectively. In comparison, the 22 seismic events reported by the USGS catalog on the first day of the eruption reach a total seismic moment of about 2.35×10^{17} N · m, corresponding to a seismic magnitude Mw = 5.5. This yields a geodetic/seismic ratio ranging from 13 to 17, depending on the model. Such high moment ratios have been observed in other volcanic areas worldwide and authors have suggested that a large proportion of the stress energy is likely released aseismically rather than by brittle failure (Langbein et al., 1993; Pedersen et al., 2007). Note that moment ratios must be invoked with caution since they are determined with an order of magnitude of uncertainty (Pedersen et al., 2007).

7.3. Role of a branch of the LOFS based on surface observations

Our kinematical models (section 6) suggest that right-lateral normal slip motion along a branch fault of the LOFS played an essential role during the explosive phase of the 2011 eruption. This scenario differs from that of Wendt et al. (2017) of a closing dyke with a left-lateral normal strike-slip motion along the northern flank of the graben. As mentioned above, the activation of a LOFS branch is strongly supported by independent seismic data, structural field observations and available petrological data (section 2). In addition, structural and satellite data show *en-échelon* fracture segments and aligned ground cracks in directions parallel to an overlapping cone structure striking N18°W (Schipper et al., 2013). The coincident location and strike of these structures with the buried fault obtained in our inversion model, strengthens this interpretation. Finally, failure along a fault plane is also invoked by Castro et al. (2013) to explain the transport of magma from depth to the vent at very slow rates (∼1 cm/yr).

Slip motion along the LOFS also provides insight into the transition of the eruption style from explosive to effusive: the coincident orientation of the vents, the inverted fault plane and the location of the seismic swarm during the explosive phase all indicate that this fault zone itself may have been the channel along which the magma rose to the surface. Based on the coincident depth of the reservoir inferred from petrological data (2-5 km) and that of the shallow seismicity reported two days before the eruption (2-6 km), Castro et al. (2016) suggested that rock fracturing occurred in association with the creation of a dyke-like conduit that fed the vent. Therefore, we propose that the transition from the explosive to the effusive phases was associated with the transition from a shear-slipping fracture that allowed the magma to degas, to its opening as a dyke through which magma withdrawal occurred and reached the surface. A similar mechanism is also suggested for caldera collapses within strike-slip tectonic regimes (e.g., Holohan et al., 2008).

7.4. Possible mechanisms triggering the 2011 eruption

Our models of a magmatic overpressurization induce dilatation at the shallowest tip of the reservoir located beneath the Cordillera Nevada Caldera. Such dilatational domains can mobilize fluids and promote seismicity (references in section 5.2). Similarly to Lundgren et al. (2020) and Zhan et al. (2019), we suggest that the seismicity reported between 2007-2011 beneath the Cordillera Nevada Caldera resulted from such a dilatation induced by magmatic injection during the pre-eruptive period (Fig. 4B). Our models also show that constriction around the inflating reservoir does not facilitate magmatic fluid flow towards the surface (Fig. 4C-D), and thus rather inhibits an eruption. Whereas the lack of substantial pre-eruptive inflation observed by InSAR in the two years prior
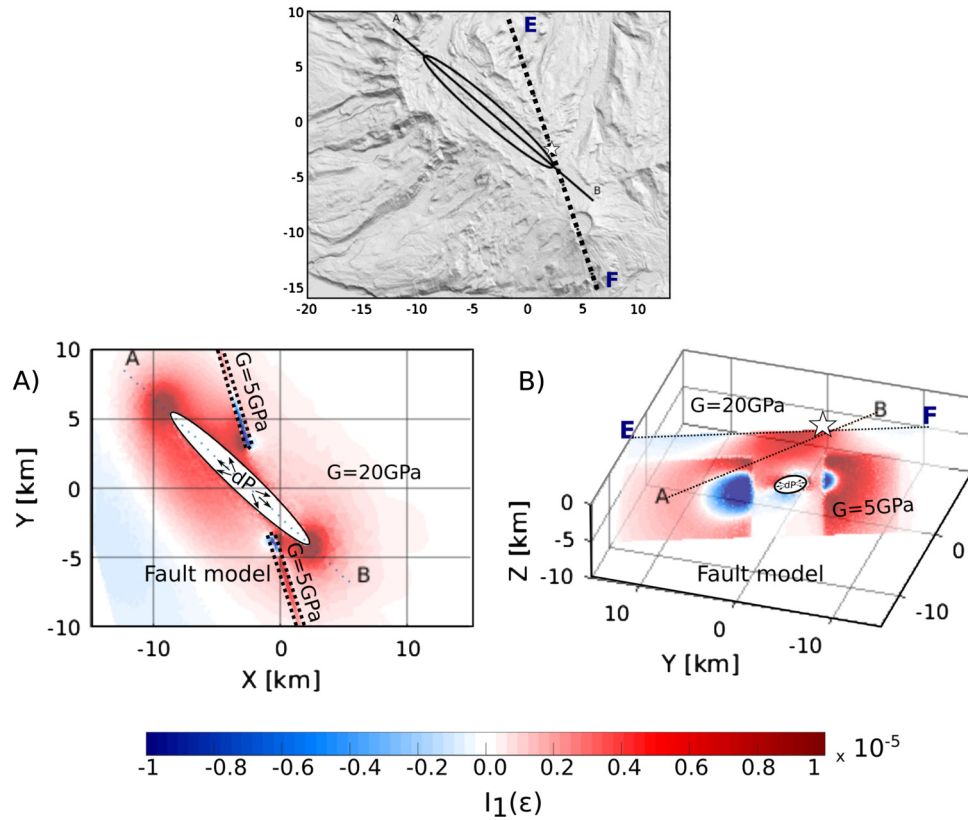
Fig. 7. Computed first invariant of the strain ($I_1(\varepsilon)$) with *Adeli*, for an overpressurized prolate-spheroidal cavity that best fits the pre-eruptive surface displacements considering a weak crustal fault zone near the cavity, with $G = 5$ GPa, and an elastic bedrock with $G = 20$ GPa. A) Sub-horizontal plane view following the inclined major axis of the cavity. B) Vertical view of the fault plane along profile EF. Areas of dilatation shown in red.

to the eruption leads us to discard magma supply from depth as the 2011 eruption trigger, we cannot exclude the possibility that a short-lived pre-eruptive inflation was compensated by co-eruptive deflation in a single orbital cycle. The other scenario of a caldera collapse alone, which would have triggered reservoir withdrawal and the eruption of magma, requires a tensile state of stress across the caldera-graben structure, and normal slip along the caldera and graben walls. This is inconsistent with the regional interseismic state of compression expected at PCCVC. While Gudmundsson (1998) argued that extension could be induced by flexural doming of a deeper pressure source under the shallow chamber, here there is no evidence of large-scale precursory inflation at PCCVC. However, once again we cannot exclude that the amplitude of ground displacement induced by a deep source was below the accuracy of radar sensors, or was compensated by the co-eruptive deflation.

Several studies have suggested that the seismic cycle of subduction megathrusts plays a key role in modifying the stress field in the overriding plate and promoting transient tensile stresses (Walter and Amelung, 2007). While Lara et al. (2006) proposed that the recurrent shearing of pre-existent faults at PCCVC causes transient stress field rotations, promoting the ascent of magma within coeval tensile conditions, there is no evidence that the 2011 Cordón Caulle eruption was directly triggered by the 2010 Maule megaearthquake: first, the latter occurred far away (∼500 km to the north), and second, according to Bonali et al. (2015) it rather exerted a clamping of the PCCVC area, tending to impede any eruption.

Consequently, we need to search for another triggering mechanism to the 2011 Cordón Caulle eruption.

7.5. The slipping LOFS branch hypothesis

The last mechanism that could lead to draining of the magma chamber would be slip motion along a branch of the LOFS. Hence, we investigate now, how motion along a branch-fault of the LOFS could have triggered the eruption by setting up additional 3D models that explore such a fault-reservoir interaction (mesh shown in Appendix C.3). First we check the response of this configuration to a pre-inflation with $\Delta P = 32$ MPa: assuming elastic behavior, Fig. 7 shows constriction in the fault domains closest to the reservoir, which are squeezed by the expanding stiffer surrounding bedrock. However, further away along the fault domain, constriction switches to dilatation (positive volumetric strain); this may increase porosity, favor the release of interseismic pre-existing stress and drive magmatic fluid pathways (e.g. Ruz-Ginouves et al., 2021). Then considering elasto-plasticity, even low fault strength values such as T=1 MPa and C=5 MPa generate only a restricted plastic domain. Inflation does not trigger surface failure and is too small to be detected by InSAR observations.

Second, we apply slip motion along the walls of these fault zones, with magnitudes consistent with the geodetic moment obtained from the inversions (section 6.2). This fault activation promotes dilatation and constriction at the edges of the fault planes (Fig. 8A). At reservoir depths, the induced dilatation exceeds by ∼3 times the dilatation predicted during the pre-eruptive period (Fig. 5A vs. Fig. 8A), and the shear stress is potentially ∼7 times greater (Fig. 5C vs. 8B). With cohesion and tensile strength identical to the pre-eruptive configuration, this elasto-plastic model now predicts shear failure along the entire fault zone, and tensile failure in the bedrock between the fault zone and the reservoir, Fig. 8C. In contrast to the pre-eruptive inflation models, this plastic dilatation
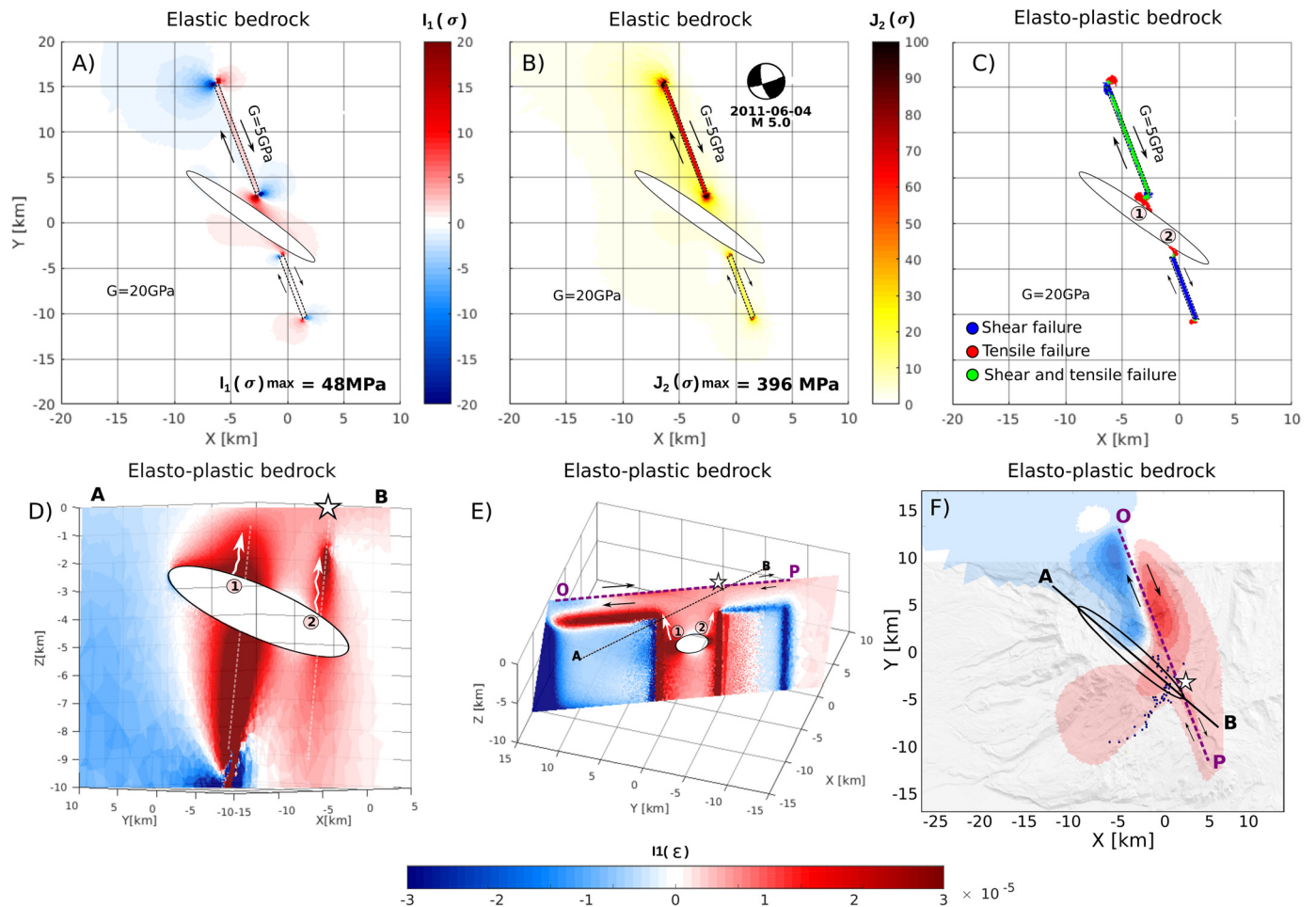
Fig. 8. Patterns of stress and deformation using *Adeli* when a dextral motion of 2.5 m and 75 cm is applied along the north-western and south-eastern walls of a LOFS branch-fault zone respectively, to the east of the reservoir (not overpressurized here). A-B) First and second stress invariants assuming an elastic bedrock, viewed along a sub-horizontal plane inclined along the reservoir's major axis. Note the reduced color palette. Maximum dilatation occurs at the fault's edges and around the reservoir nearby. Shear stress is maximum inside the fault zones and at their edges. C) Failure pattern assuming an elasto-plastic bedrock: plastic failure inside the two fault zones and tensile failure throughout the bedrock connecting them to the reservoir, from which dyking can be generated along two channels (1 and 2). D-E-F) Volumetric deformation $I_1(\varepsilon)$ induced by the fault motion, assuming an elasto-plastic bedrock and along vertical profiles AB and OP. D-E) Magma potentially rises following one of the two highly dilatational channels (1 and 2). Dotted white lines indicate the fault zones intersections with profile AB. F) Volumetric deformation $I_1(\varepsilon)$ at the top surface. The 2011 eruptive vent (white star) and the pre-eruptive superficial seismicity (blue points, Wendt et al., 2017) are located within the dilating area near the reservoir and the fault zone intersection.

domain develops through the bedrock and connects the reservoir with the surface, in the SE part of the PCCVC where the vent actually occurred (Fig. 8D-E-F). This sub-vertical dilatational domain can be interpreted as a channel that opens the bedrock pore space from which magmatic fluids can migrate all the way up to the surface (pathways 1-2 in Fig. 8D-E-F). Dilatation at the surface encompasses the location of the swarm of shallow seismicity reported by Wendt et al. (2017) a few days before the eruption (Fig. 8F). We note that pathway (1) may have been impeded with respect to pathway 2 because first, constriction during the pre-eruptive phase counter-acts dilatation, and second, constriction close to the surface impedes magma out-flow.

The activation of a NNW-striking LOFS branch stands as the best candidate scenario to explain the 2011 Cordón Caulle eruption. In terms of timing, it is difficult to discern the exact moment when slip may have started on this fault. Based on the change in location of seismicity presented by Wendt et al. (2017) we suggest that it may have occurred a few days before the eruption. Our hypothesis is also consistent with Lara et al. (2006)'s proposition that shearing of pre-existent faults promotes magma ascent within

transient tensile conditions, in a way similar to other studies (e.g. Díez et al., 2005).

7.6. Triggering of historical eruptions

The last three eruptions at PCCVC occurred at different places, along the ring faults of the Cordillera Nevada Caldera in 1921 and along the opposite edges of the Cordón Caulle graben in 1960 and in 2011 (Fig. 1). Geological mapping shows that this pattern is repeated for the older units thus evidencing a long-term behavior. Our simulations show that when considering a sufficient overpressure in the reservoir, the connection of the plastically yielded domain between the reservoir and the surface occurs in the NW section of the PCCVC, under the Cordillera Nevada Caldera and the NW portion of the graben. Consequently, we suggest that the 1921 eruption and those previously fed from vents located along the ring faults likely had a dominantly magmatic origin.

While the 2011 eruption would have responded to a combination of magmatic and tectonic forcing, none of the mechanisms explored here explain the location of the 1960 eruption at PCCVC, which occurred along the graben's southern wall. This erup-

tion occurred only 36 hours after the Mw 9.5 Valdivia earthquake (Barrientos, 1994), just in front of the major rupture zone. In relation to the argument cited above that the seismic cycle is able to modify the regional stress field (Manga and Brodsky, 2006; Walter and Amelung, 2007), Lara et al. (2004) argued that co-seismic extension inland promoted reshearing of the NW faults along the graben, and generated a transient transtensional pattern that favored the eruption. Moreover, the 2015 eruptive activity at Nevados de Chillan was also linked to the 2010 Maule earthquake (Lupi et al., 2020). Future modeling should investigate the rotation of the regional stress field due to far-field subduction earthquakes. The constraints provided by our models here combined with those of Lara et al. (2004) feed the discussion about remote triggering of volcanic eruptions.

8. Conclusions

In this study we used geodetic data recorded before, during and after the 2011 Cordón Caulle eruption, to understand the mechanical conditions associated with its eruptive cycle. We found that the ground displacements observed before and after the eruptive event can be linked with a similar inflating source, suggesting that the geometry of the shallow plumbing system regained its pre-eruptive shape. Nevertheless, the subsidence observed during the explosive phase of the eruption requires an additional cause, for which we tested two hypotheses implying fault slip motion.

Our results indicate that part of the observed subsidence during the explosive phase was due to dextral-slip motion along a pre-existing NNW-striking branch-fault of the LOFS. The pre-eruptive magmatic inflation potentially weakened this branch-fault, which would have been reactivated before the eruption.

We relate this dextral-strike slip motion to the earthquake swarm including the Mw 5.0 earthquake that occurred quasi-simultaneously with the onset of the eruption. The greater geodetic moment deduced from our analysis than the seismic moment released by the swarm suggests that this slip motion was mainly aseismic. However, the lack of continuous GNSS recording stations in the vicinity of LOFS prior to the eruption makes it impossible to determine a precise timing of this slow slip event. We propose that this largely aseismic slip motion changed the local stress state from compressive to tensile within the volcanic complex, leading to magma rising to the surface.

Although standard elastic models provide good information to constrain the geometry, location and overpressure conditions on a magma reservoir from the inversion of observed surface displacements, 3D elasto-plastic models accounting for rheological heterogeneities help assessing the mechanical state, the potential weakening induced by magmatic injection, and the tectonic trigger of explosive eruptions. In that line, 3D numerical methods accounting for non-linear (poro-visco-elasto-plasticity) rheology will soon become essential to move forward in understanding silicic eruptions.

CRediT authorship contribution statement

C. Novoa: Conceptualization, Methodology, Software, Visualization, Writing – original draft, Writing – review & editing. **M. Gerbault:** Conceptualization, Funding acquisition, Methodology, Supervision, Validation, Writing – review & editing. **D. Remy:** Conceptualization, Funding acquisition, Methodology, Resources, Software, Supervision, Validation, Writing – review & editing. **J. Cembrano:** Funding acquisition, Validation, Writing – review & editing. **L.E. Lara:** Resources, Writing – review & editing. **J. Ruz-Ginouves:** Visualization, Writing – review & editing. **A. Tassara:** Writing – review & editing. **J.C. Baez:** Resources, Writing – review & editing. **R. Hassani:** Software, Writing – review & editing. **S. Bonvalot:** Funding

acquisition, Validation, Writing – review & editing. **R. Contreras-Arratia:** Validation, Writing – review & editing.

Declaration of competing interest

The authors declare that they have no known competing financial interests or personal relationships that could have appeared to influence the work reported in this paper.
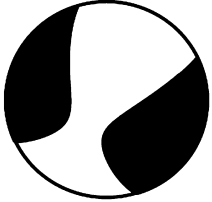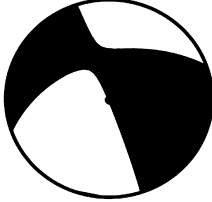
Acknowledgements

Appendix A. 04/06/2011 earthquake mechanism

The GCMT project provided a solution for the largest seismic event on the day of the eruption (at the top of Table A.1). In order to check the validity of the solution, we used teleseismic data from the IRIS repository to perform a moment tensor inversion under a probabilistic approach using the GROND software (Heimann et al., 2018). We used only waveforms with a good signal-to-noise ratio, ensuring the best possible data fit. The best solution is shown at the bottom of Table A.1. It is located on the fault trace south of the PCCVC at 7 km depth. It also shows a dextral strike-slip focal mechanism with 10% of non-double couple component.

Appendix B. InSAR processing method

All the interferograms used in this study (Table B.1) were processed with the InSAR Scientific Computing Environment (ISCE) software (Rosen et al., 2012). We used the 1 arcsec Shuttle Radar Topographic Mission digital elevation model (SRTM) to remove the topographic contribution and to provide a geographic framework (UTM WGS84) for the interferograms. We used a weighted power spectral density filter (Goldstein et al., 1988) to filter the interferograms which were later unwrapped using an implementation of the Statistical cost, Network-flow Algorithm for Phase Unwrapping −SNAPHU (Chen and Zebker, 2002). The main difficulty to carry out InSAR data analysis in the study area arises from the temporal behavior of the interferometric coherence. Snow cover prevents computing interferograms during the winter months from May to November. Furthermore, interferograms from SAR images acquired during the five months of summer, show generally a reduced spatial extent of coherent area. Consequently, despite a large number of available interferograms, few interferograms are suitable for InSAR. Many coherent interferograms reveal large-wavelength phase signals or phase signals varying with topography. As the magnitude of these signals is not correlated with the perpendicular baseline,

Table A.1
The best focal mechanism solution for the seismic event on the day of the eruption. The top of the table corresponds to the GCMT solution and the bottom corresponds to our solution.

| Solutions	Date and time	Geometrical parameters	Focal Mechanism	Mw
GCMT solution	04-06-2011 16:28:47	Hypocentre: −40.59, −72.22 Depth: 21.2 km **NP1:** Strike: 65° Dip: 77° Rake: −27° **NP2:** Strike: 164° Dip: 74° Rake: −165°		5.0
Our solution	04-06-2011 16:28:47	Hypocentre: −40.62143, −72.11687 Depth: 7.1 km **NP1:** Strike: 250° Dip: 44° Rake: −1° **NP2:** Strike: 340° Dip: 89.5° Rake: −130°		5.0
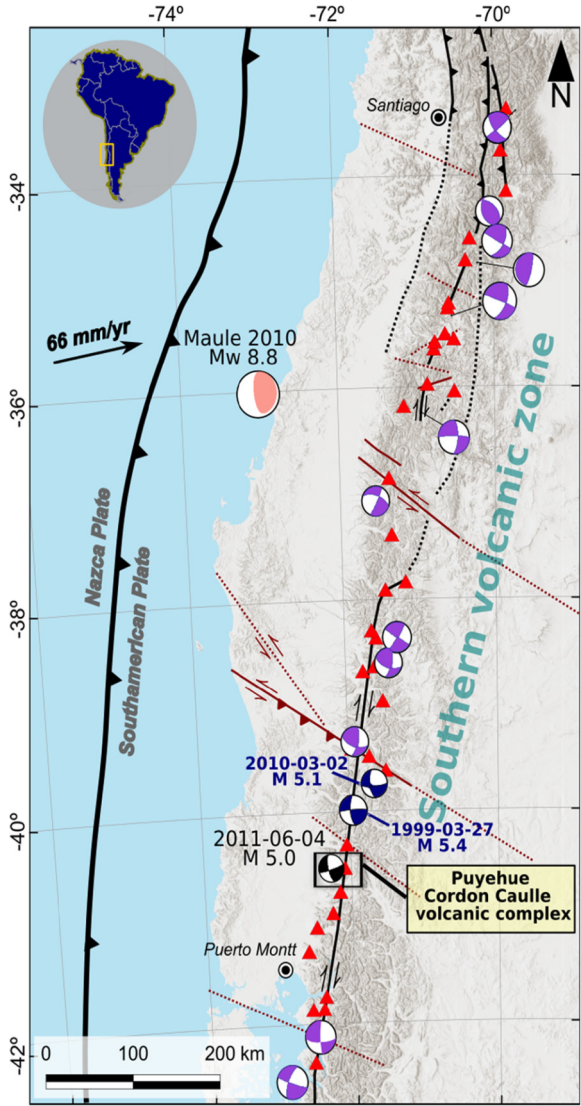
Fig. A.1. Regional scale map of the Southern Volcanic zone of Chile, displaying main recent earthquakes, fault traces and volcanic complexes. Momentum tensors and their focal mechanisms were extracted from the gCMT catalogue and includes crustal events of M ≥ 5 (purple beach balls). The blue beach balls indicate crustal events near the PCCVC, which have a similar focal mechanism to that which occurred on the day of the eruption (indicated by a black beach ball). The 2010 Mw 8.8 Maule is indicated by the pink beach ball. Most of these earthquakes were extracted from the collection of superficial crustal events compiled by Siefeld et al., 2019; as well as the trace of the LOFS which is indicated by the black line with a dextral motion. ATF are indicated by the red lines.

Table B.1
InSar data.

Satellite	Orbite	Track	Start date	End date
ALOS1	Ascending	118	2007/06/23	2011/02/16
ALOS1	Ascending	119	2007/07/10	2011/03/05
ALOS2	Ascending	176	2016/07/20	2018/07/14
Sentinel-1	Ascending	164	2015/02/25	2018/12/30
Sentinel-1	Descending	83	2014/11/16	2018/09/20
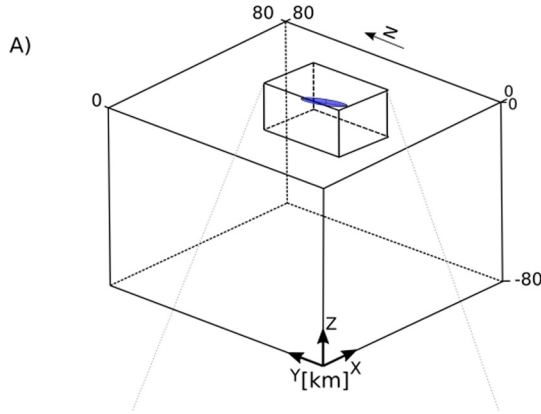
Fig. C.1. Homogeneous model. The entire mesh domain, contains only a cavity in the homogeneous case, which has the geometry of the prolate-spheroidal magma reservoir. The small parallelepiped display above only serves to separate higher and lower resolution domains.

Fig. C.2. Caldera-graben mesh model.

Fig. C.3. Caldera-graben mesh model.

we considered that they are produced either by a change in variation of water vapor or by a pressure change. To mitigate the phase delays we corrected the interferograms using a simple empirical function that correlates phase and topography and a ramp function (linear function and a phase offset) to account for long wavelength signals after masking the area affected by displacements. This step also enabled us to estimate the uncertainty for each interferogram, and to make phase values comparable in both space and time.
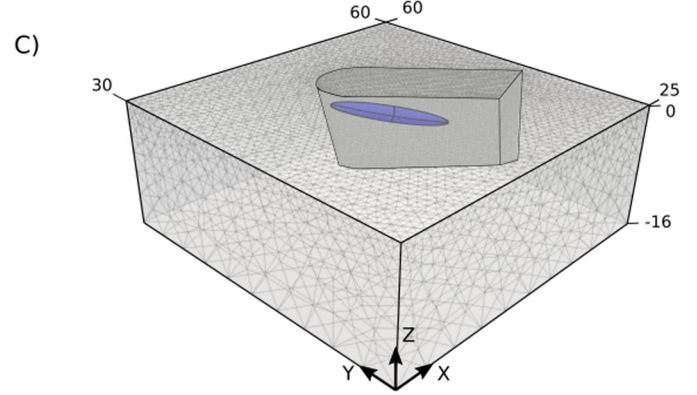
Appendix C. Numerical domain setup for the three Adeli models

C.1. Homogeneous model

The model domain consists of a 3D block of dimensions $80 \times 80 \times 60$ km and is meshed with the Gmsh free software (gmsh.info, Geuzaine and Remacle, 2009), with a resolution increasing from about 90 meters at the cavity walls to 8 km at the model borders. The domain borders are set free-slip except for the top free surface and the magma cavity, which remains un-meshed and whose walls are loaded with incremental overpressure (ΔP) (Fig. C.1).

C.2. Caldera-Graben model

The geometrical parameters determining the Cordillera Nevada Caldera and the northern and southern graben's walls are set based on mapped surface structures (Lara et al., 2006). Then, we extrapolate these structures at depth following the inner dipping boundaries of the caldera-graben walls suggested by Sepúlveda et al. (2005) from gravity modeling. The dip angle is strongly constrained by the structure of the graben and ranges between 90 to 60 °, therefore we choose a mean value of 75°. The resulting mesh is displayed Fig. C.2.
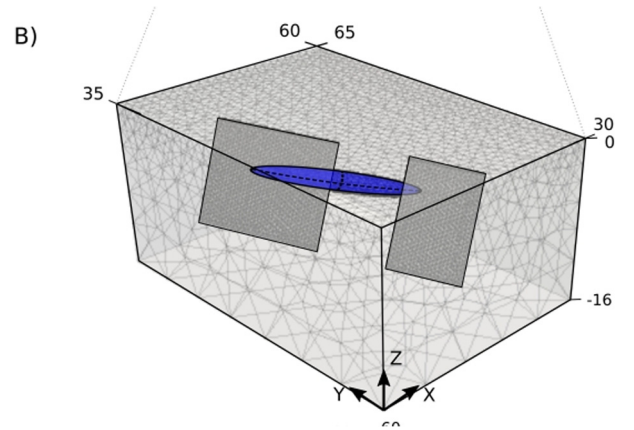
C.3. LOFS fault model

Fault volumes are meshed with a thickness 300 m and extend over 15 km using the best fit geometry obtained from inversions of section 6 and assuming G = 5 GPa and 20 GPa in the fault volume and bedrock, respectively. In Fig. 7 an overpressure is applied at the walls of the cavity whereas in Fig. 8 a constant tangential velocity is applied along the western wall of the fault zones (Fig. C.3).

Appendix D

Complementary numerical models illustrating the patterns of plastic failure resulting from the inflation of a cavity embedded in a homogeneous crust. While the main text assumes a Young modulus $E = 50$ GPa ($G = 20$ GPa, Fig. 6, $T = 4$ MPa and $C = 20$ MPa), cases here have $E = 12.5$ GPa, $T = 1$ MPa and $C = 5$ MPa, variable friction angle ϕ, gravity acceleration $\boldsymbol{g}$ and loading overpressure ΔP.
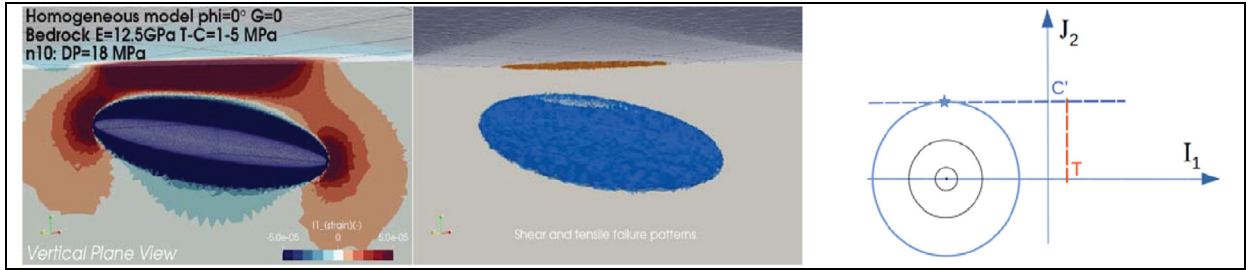
a) g=0 and ϕ=0°, plastic connection at ΔP=16 MPa (compare with Fig. 5):
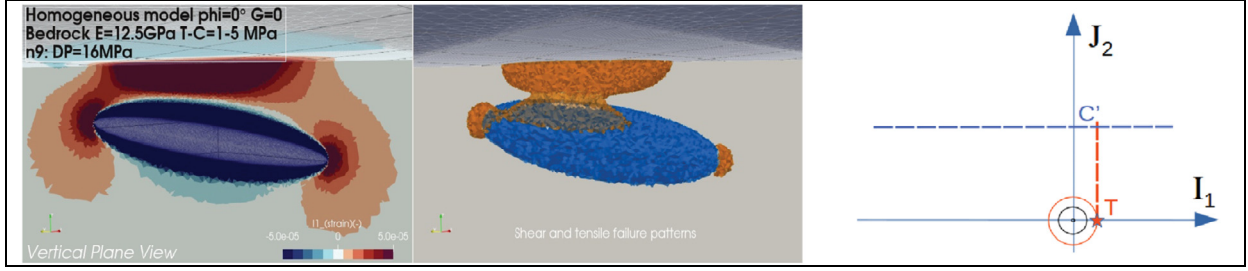
b) g=0 and ϕ= 30°, plastic connection occurs at ΔP=20 MPa, later than in **a)**:
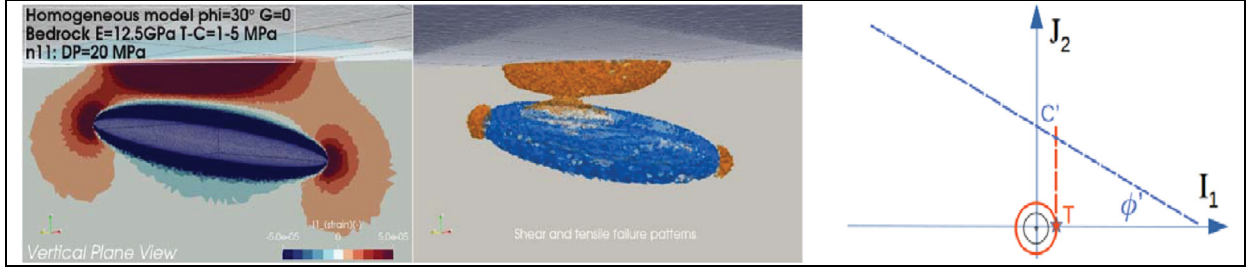
c) g=10 m/s² and ϕ=0°, for ΔP=18 MPa: tensile failure is inhibited (except top), shear failure occurs.

d) g=10 m/s² and ϕ=30°, at ΔP= 34 MPa, shear and tensile failure remain impeded (except top).
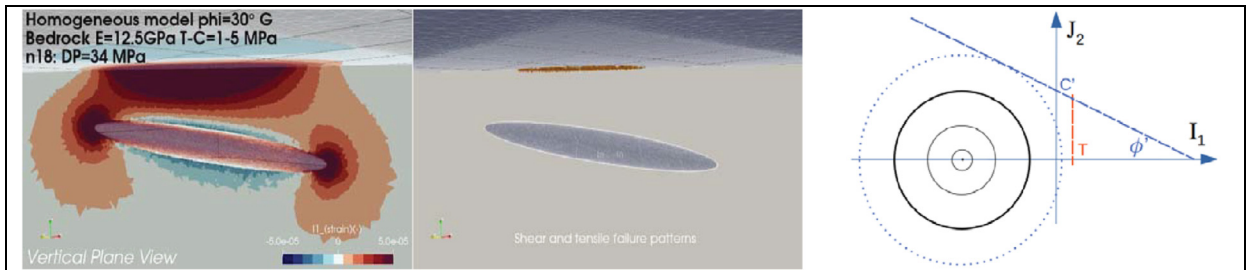

Fig. D.1. Complementary models displaying distinct patterns of dilation/constriction (left, vertical section parallel to the magma reservoir long axis), tensile and shear failure mode patterns (middle, 3D view), and stress state upon loading in the (I1, J2) stress state (to the right). Four cases with distinct rock mass properties: a) without gravity and frictionless, b) without gravity and friction angle 30°, c) with gravity and frictionless, d) with gravity and friction angle 30°.

The figures above display in vertical cross section, to the left $I_1(\varepsilon)$ (dilatation in red, color scale ranging from -5.10^{-5} to $+5.10^{-5}$), and in the center, domains of tensile (in red) and shear failure (in blue) (Fig. D.1). To the right, a schematic Mohr-circle/stress amplitude plot is drawn, with the first and second stress invariants in abscissa and ordinates. This representation illustrates where failure can occur (stars) for shear and tensile failure, with tensile strength T and equivalent cohesion and friction: $C' = \frac{6C\cos(\phi)}{3-\sin(\phi)}$, $\phi' = arctan\left(\frac{6C\sin(\phi)}{3-\sin(\phi)}\right)$.

a) with $g = 0$ gravity and friction $\phi = 0°$, this case compares with the main text homogeneous case (Fig. 5) except that the bedrock here has $G = 5$ GPa instead of $G = 20$ GPa. Hence, connection of the failure pattern between the cavity walls and the surface

occurs for $DP = 16$ MPa, instead of 64 MPa in the main text case. At any location point in the model the initial stress $I_1 = 0$, and the stress circle increases (black circles) with increasing reservoir overpressure; tensile failure occurs first (red star).

b) with $g = 0$ and friction $\phi = 30°$ (depth dependent condition for shear failure), the deformation and failure patterns are very similar to **a)** with tensile failure still prevailing over shear failure.

c) with $g = 10$ kg/m³ and friction $\phi = 0°$, I_1 at any depth z includes the gravity component $\rho.g.z$, shifting the stress state to negative abscissas along the "Mohr-circle". Hence, the applied magma overpressure needs to overcome this constrictional stress for the stress field to reach the failure envelope. Since the shear failure threshold is low ($\phi = 0°$), shear failure occurs around the
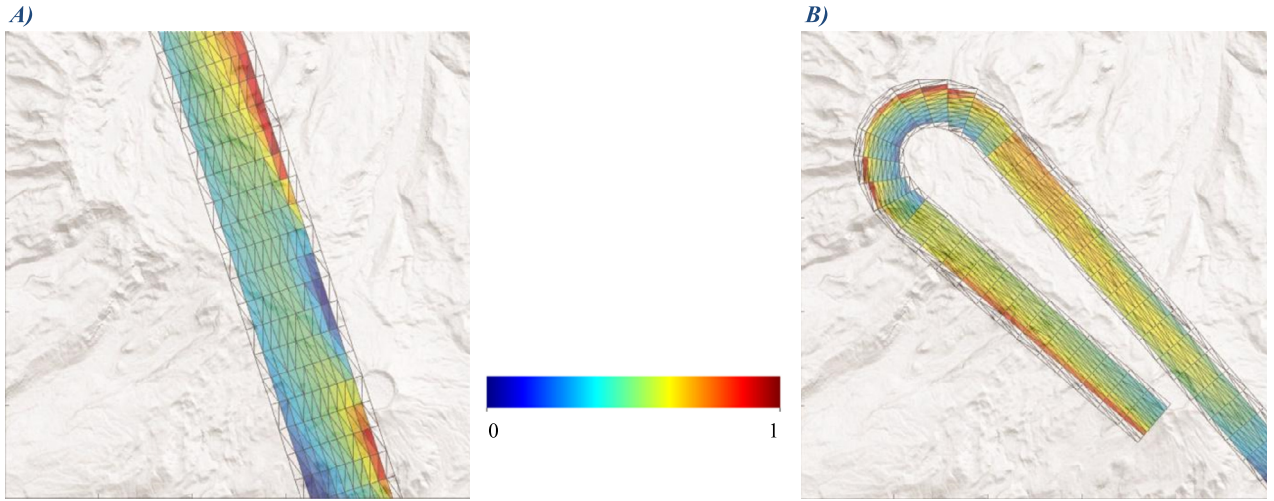
A)

B)

Fig. E.1. Spatial resolution of the models. A) Spatial resolution of the LOFS model. Normalized contribution of each patch to the total displacement of assuming a homogeneous slip with rake fixed to −165°. B) Spatial resolution of the Caldera-Graben model assuming a normal slip for the Caldera and right lateral slip for the flank of the graben.

inflating cavity while tensile failure is restricted to the surface ($z < 1$ km).

d) with $g = 10$ kg/m^3 and $\phi = 30°$, both shear and tensile failure thresholds require greater overpressure than in previous cases. The domain remains elastic except at the very top surface where tensile failure is still allowed.

The simulations in the main text assume zero-friction and zero-gravity, as in case **a)** here, and correspond to the extreme situation in which the entire crustal domain is saturated with lithostatic pore-fluid pressure (the effective mean stress vanishes, Hubbert and Rubey, 1959) we are in the most favorable conditions for bedrock shear and tensile failure at lowest possible applied overpressure. Considering friction without gravity (case **b)** does not influence much the results since it only raises the shear failure yield envelope with depth. However, as soon as gravity is accounted for, the mean stress (I_1) is shifted to negative values. Zero-friction retains the shear failure threshold to $2C$, but 30° requires the overpressure to achieve about $1/2.\rho.g.z$ for the reservoir walls to fail (Gerbault et al., 1998). Hence at the shallowest reservoir tip where $z = 3$ km, the required overpressure already would have to exceed ∼40 MPa.

Appendix E. PCAIM and resolution tests for the Caldera-Graben and the LOFS models

To solve for the slip distribution on the different fault planes used in this study, we used Principal Component Analysis-based Inversion Method (PCAIM) software package. In our models the slip distribution **S** in elastic medium is related to the surface displacements through

$$X_{dat} = GS \tag{E.1}$$

where G is the Green function operator that gives the displacement at the measuring sites resulting from a unit slip applied on the fault and X_{dat} are the InSAR observations. To compute the Green functions, we consider point sources embedded in a homogeneous elastic half-space [Okada, 1992], assuming a Poisson coefficient of 0.25.

In the PCAIM algorithm, we solve for

$$\begin{pmatrix} X_{dat} \\ 0 \end{pmatrix} = \begin{pmatrix} G \\ \gamma \Delta \end{pmatrix} S \tag{E.2}$$

The Laplacian matrix Δ is a smoothing operator regularizing the inversion and γ the associated parameter. The main principle of PCAIM can be found at: http://www.tectonics.caltech.edu/resources/pcaim/ and examples of applications can be found in the works of Lin et al. (2010), Perfettini and Avouac (2014), Remy et al. (2014).

Here, we detail different resolution tests that we have performed to solve for the slip distributions on the fault planes used in our study. To quantify the spatial resolution of our slip models, we compute the contribution of each patch to the total displacement of the InSAR dataset using a approach similar to that used by [Loveless and Meade, 2010; Perfettini and Avouac, 2014]. The contribution of each patch is computed considering the cumulated displacement amplitude over all observation sites due a unit of slip on this given patch. Next, the resulting field is normalized to have values between 0 and 1. The contribution of each patch to the total displacement is shown in Fig. E.1. Patches with no color are those for which slip is not allowed.

The LOFS slip model, constrained by InSAR measurements is shown in Fig. E.1.A. As expected, the normalized contribution of the patches decreases with depth and in the region of Puyehue where no InSAR measurements are available. In the same way, the normalized contribution of the patches for the Caldera-Graben slip model decreases for the patches located in the eastern part of the study area (Fig. E.1.B).

The spatial resolution of our model was further tested with additional resolution tests where we impose an initial slip distribution. For the LOFS model, this distribution consists of three rectangular asperities of about 4 km with unit slip. The distribution for the Caldera-Graben model consists of five rectangular asperities of about 3 km with unit slip (Fig. E.2). To the resulting modeled displacement we add a Gaussian noise with variance of 1.10^{-4} m^2.

The ability of our models to recover the imposed pattern, considering two values of the smoothing parameter is shown in Fig. E.3. Not surprisingly, rough models always allow a better reconstruction of the initial slip distribution. The Caldera-Graben model shows a lower ability to recover the imposed slip pattern in the eastern part of the fault plane, even using a low value (rough model) of the smoothing parameter.

References

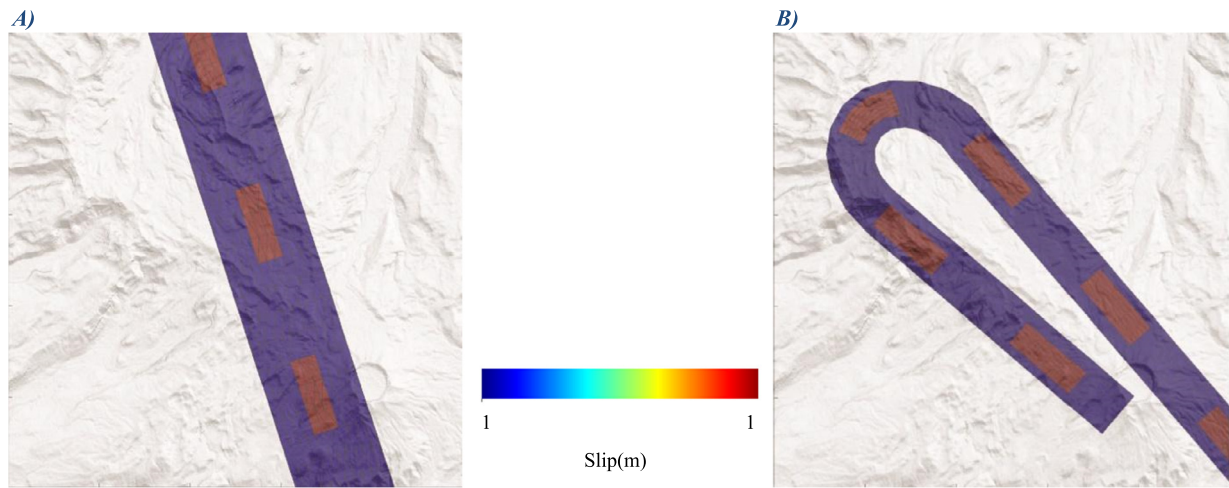Barrientos, S.E., 1994. Large thrust earthquakes and volcanic eruptions. Pure Appl. Geophys. https://doi.org/10.1007/BF00875972.

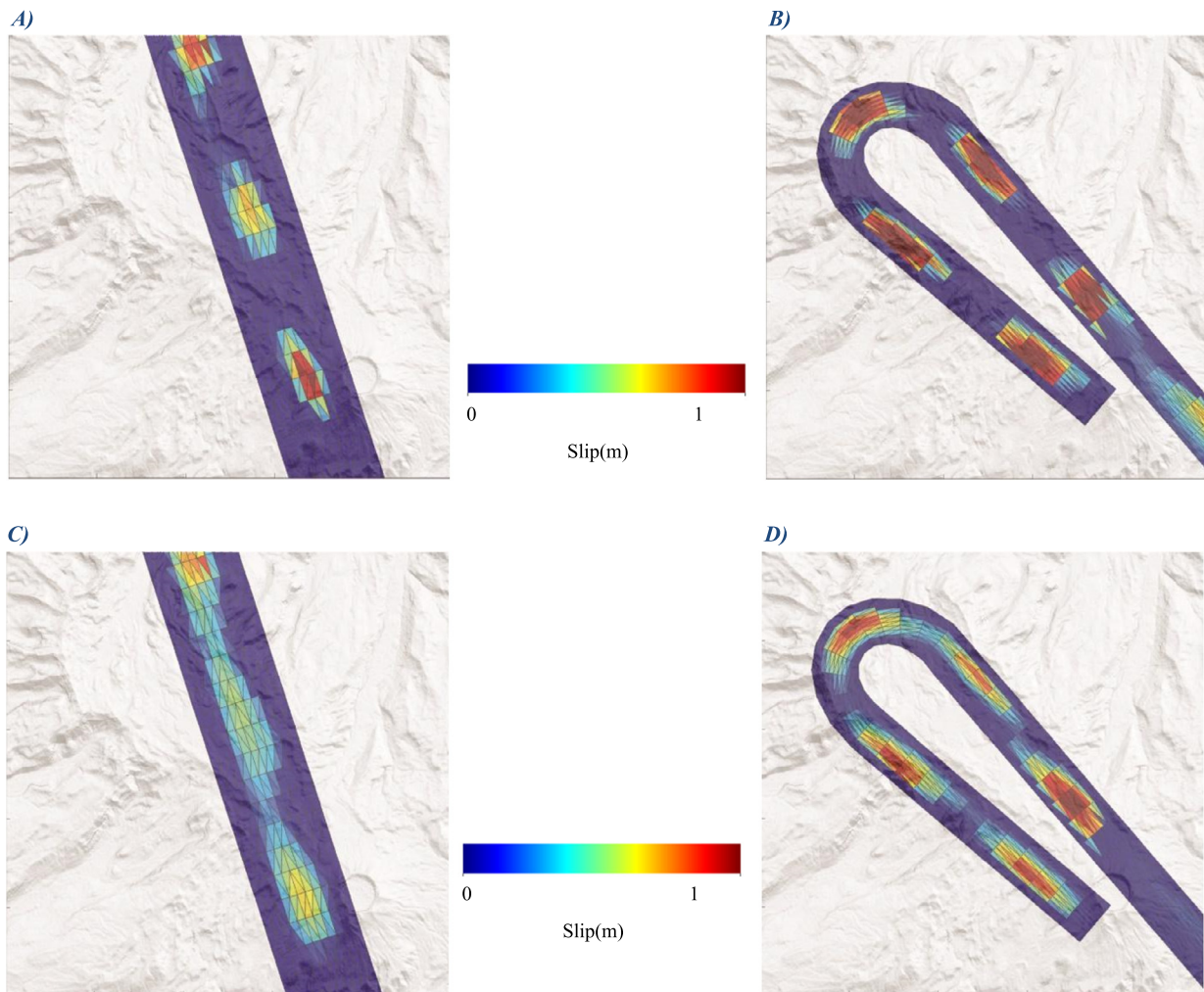**Fig. E.2.** Synthetic Models. A) LOFS model. B) Caldera-Graben model.

Fig. E.3. Recovered slip distributions. A and B) Using a low value of the smoothing parameter. The resulting rms for both model is 0.01. C and D) Smooth models by increasing the smoothing parameter. The resulting rms for these models are 0.014 and 0.015 m, respectively.

Bertin, D., Lara, L.E., Basualto, D., Amigo, A., Cardona, C., Franco, L., Gil, F., Lazo, J., 2015. High effusion rates of the Cordõn Caulle 2011-2012 eruption (Southern Andes) and their relation with the quasi-harmonic tremor. Geophys. Res. Lett. https://doi.org/10.1002/2015GL064624.

Bonadonna, C., Pistolesi, M., Cioni, R., Degruyter, W., Elissondo, M., Baumann, V., 2015. Dynamics of wind-affected volcanic plumes: the example of the 2011 Cordón Caulle eruption, Chile. J. Geophys. Res., Solid Earth. https://doi.org/10.1002/2014JB011478.

Bonali, F.L., Tibaldi, A., Corazzato, C., 2015. Sensitivity analysis of earthquake-induced static stress changes on volcanoes: the 2010Mw 8.8 Chile earthquake. Geophys. J. Int. https://doi.org/10.1093/gji/ggv122.

Castro, J.M., Cordonnier, B., Schipper, C.I., Tuffen, H., Baumann, T.S., Feisel, Y., 2016. Rapid laccolith intrusion driven by explosive volcanic eruption. Nat. Commun. https://doi.org/10.1038/ncomms13585.

Castro, J.M., Schipper, C.I., Mueller, S.P., Militzer, A.S., Amigo, A., Parejas, C.S., Jacob, D., 2013. Storage and eruption of near-liquidus rhyolite magma at Cordón Caulle, Chile. Bull. Volcanol. 75 (4), 1–17.

Cayol, V., Cornet, F.H., 1998. Effects of topography on the interpretation of the deformation field of prominent volcanoes – application to Etna. Geophys. Res. Lett. 25 (11), 1979–1982.

Cembrano, J., Lara, L., 2009. The link between volcanism and tectonics in the southern volcanic zone of the Chilean Andes: a review. Tectonophysics. https://doi.org/10.1016/j.tecto.2009.02.038.

Cembrano, J., Hervé, F., Lavenu, A., 1996. The Liquiñe Ofqui fault zone: a long-lived intra-arc fault system in southern Chile. Tectonophysics 259 (1–3), 55–66.

Cerpa, N.G., Araya, R., Gerbault, M., Hassani, R., 2015. Relationship between slab dip and topography segmentation in an oblique subduction zone: insights from numerical modeling. Geophys. Res. Lett. https://doi.org/10.1002/2015GL064047.

Chen, C.W., Zebker, H.A., 2002. Phase unwrapping for large SAR interferograms: statistical segmentation and generalized network models. IEEE Trans. Geosci. Remote Sens. 40, 1709–1719.

Cundall, P., 1989. Numerical experiments on localization in frictional materials. Ing.-Arch. 59 (2), 148–159.

Delgado, F., 2020. Rhyolitic volcano dynamics in the Southern Andes: contributions from 17 years of InSAR observations at Cordón Caulle volcano from 2003 to 2020. J. South Am. Earth Sci. https://doi.org/10.1016/j.jsames.2020.102841.

Díaz, D., Zúñiga, F., Castruccio, A., 2020. The interaction between active crustal faults and volcanism: a case study of the Liquiñe-Ofqui Fault Zone and Osorno volcano, southern Andes, using magnetotellurics. J. Volcanol. Geotherm. Res. 393, 106806.

Díez, M., La Femina, P.C., Connor, C.B., Strauch, W., Tenorio, V., 2005. Evidence for static stress changes triggering the 1999 eruption of Cerro Negro Volcano, Nicaragua and regional aftershock sequences. Geophys. Res. Lett. https://doi.org/10.1029/2004GL021788.

Gerbault, M., Poliakov, A.N., Daignieres, M., 1998. Prediction of faulting from the theories of elasticity and plasticity: what are the limits? J. Struct. Geol. 20 (2–3), 301–320.

Gerbault, M., Hassani, R., Novoa Lizama, C., Souche, A., 2018. Three-dimensional failure patterns around an inflating magmatic chamber. Geochem. Geophys. Geosyst. https://doi.org/10.1002/2017GC007174.

Geuzaine, C., Remacle, J.-F., 2009. Gmsh: a three-dimensional finite element mesh generator with built-in pre- and post-processing facilities. Int. J. Numer. Methods Eng. 79 (11), 1309–1331.

Gudmundsson, A., 1998. Formation and development of normal-fault calderas and the initiation of large explosive eruptions. Bull. Volcanol. 60 (3), 160–170.

Hassani, R., Jongmans, D., Chéry, J., 1997. Study of plate deformation and stress in subduction processes using two-dimensional numerical models. J. Geophys. Res. 102 (B8), 17951–17965.

Heap, M.J., Villeneuve, M., Albino, F., Farquharson, J.I., Brothelande, E., Amelung, F., et al., 2020. Towards more realistic values of elastic moduli for volcano modelling. J. Volcanol. Geotherm. Res. 390, 106684.

Heimann, Sebastian, Isken, Marius, Kühn, Daniela, 2018, Sudhaus, Henriette, Steinberg, Andreas, Daout, Simon, Cesca, Simone, Vasyura-Bathke, Hannes, Dahm, Torsten Grond - A probabilistic earthquake source inversion framework. V. 1.0. GFZ Data Services. https://doi.org/10.5880/GFZ.2.1.2018.003.

Holohan, E.P., Van Wyk de Vries, B., Troll, V.R., 2008. Analogue models of caldera collapse in strike-slip tectonic regimes. Bull. Volcanol. https://doi.org/10.1007/s00445-007-0166-x.

Hubbert, M. King, Rubey, W.W., 1959. Role of fluid pressure in mechanics of overthrust faulting: I. Mechanics of fluid-filled porous solids and its application to overthrust faulting. Geol. Soc. Am. Bull. 70 (2), 115–166.

Jay, J., Costa, F., Pritchard, M., Lara, L., Singer, B., Herrin, J., 2014. Locating magma reservoirs using InSAR and petrology before and during the 2011-2012 Cordón Caulle silicic eruption. Earth Planet. Sci. Lett. https://doi.org/10.1016/j.epsl.2014.03.046.

Kositsky, A.P., Avouac, J.P., 2010. Inverting geodetic time series with a principal component analysis-based inversion method. J. Geophys. Res., Solid Earth. https://doi.org/10.1029/2009JB006535.

Lamur, A., Kendrick, J.E., Eggertsson, G.H., Wall, R.J., Ashworth, J.D., Lavallée, Y., 2017. The permeability of fractured rocks in pressurised volcanic and geothermal systems. Sci. Rep. https://doi.org/10.1038/s41598-017-05460-4.

Langbein, J., Hill, D.P., Parker, T.N., Wilkinson, S.K., 1993. An episode of reinflation of the Long Valley Caldera, eastern California: 1989–1991. J. Geophys. Res. 98 (B9), 15851–15870. https://doi.org/10.1029/93JB00558.

Lara, L.E., Naranjo, J.A., Moreno, H., 2004. Rhyodacitic fissure eruption in Southern Andes (Cordón Caulle; 40.5 S) after the 1960 (Mw: 9.5) Chilean earthquake: a structural interpretation. J. Volcanol. Geotherm. Res. 138 (1-2), 127–138.

Lara, L.E., Moreno, H., Naranjo, J.A., Matthews, S., Pérez de Arce, C., 2006. Magmatic evolution of the Puyehue-Cordón Caulle Volcanic Complex (40° S), Southern Andean Volcanic Zone: from shield to unusual rhyolitic fissure volcanism. J. Volcanol. Geotherm. Res. https://doi.org/10.1016/j.jvolgeores.2006.04.010.

Lavenu, A., Cembrano, J., 1999. Compressional- and transpressional-stress pattern for Pliocene and Quaternary brittle deformation in fore arc and intra-arc zones (Andes of Central and Southern Chile). J. Struct. Geol. https://doi.org/10.1016/S0191-8141(99)00111-X.

Lin, Yu-nung Nina, Kositsky, Andrew P., Avouac, Jean-Philippe, 2010. PCAIM joint inversion of InSAR and ground-based geodetic time series: application to monitoring magmatic inflation beneath the Long Valley Caldera. Geophys. Res. Lett. 37 (23), L23301. 3 décembre.

López Escobar, Á., Cembrano, J., Moreno, H., 1995. Geochemistry and tectonics of the Chilean Southern Andes basaltic Quaternary volcanism (37-46°S). Andean Geol. https://doi.org/10.5027/andgeoV22n2-a06.

Loveless, J.P., Meade, B.J., 2010. Geodetic imaging of plate motions, slip rates, and partitioning of deformation in Japan. J. Geophys. Res., Solid Earth 115 (B2).

Lundgren, P., Girona, T., Bato, M.G., Realmuto, V.J., Samsonov, S., Cardona, C., Franco, L., Gurrola, E., Aivazis, M., 2020. The dynamics of large silicic systems from satellite remote sensing observations: the intriguing case of Domuyo volcano, Argentina. Sci. Rep. https://doi.org/10.1038/s41598-020-67982-8.

Lupi, M., Trippanera, D., Gonzalez, D., D'amico, S., Acocella, V., Cabello, C., Stef, M.M., Tassara, A., 2020. Transient tectonic regimes imposed by megathrust earthquakes and the growth of NW-trending volcanic systems in the Southern Andes. Tectonophysics. https://doi.org/10.1016/j.tecto.2019.228204.

Manga, M., Brodsky, E., 2006. Seismic triggering of eruptions in the far field: volcanoes and geysers. Annu. Rev. Earth Planet. Sci. 34, 263–291.

Mastin, L.G., Roeloffs, E., Beeler, N.M., Quick, J.E., 2008. Constraints on the size, overpressure, and volatile content of the mount st. helens magma system from geodetic and dome-growth measurements during the 2004–2006 eruption. U.S. Geol. Surv. Prof. Pap. 1750, 461–488.

McGee, L.E., Brahm, R., Rowe, M.C., Handley, H.K., Morgado, E., Lara, L.E., Turner, M.B., Vinet, N., Parada, R.M., Valdivia, P., 2017. A geochemical approach to distinguishing competing tectono-magmatic processes preserved in small eruptive centres. Contrib. Mineral. Petrol. 172 (6), 44.

Mogi, K., 1958. Relations between the eruptions of various volcanoes and the deformation of the ground surface around them. Bull. Earthq. Res. Inst. Univ. Tokyo 36, 99–134.

Novoa, C., Remy, D., Gerbault, M., Baez, J.C., Tassara, A., Cordova, L., Cardona, C., Granger, M., Bonvalot, S., Delgado, F., 2019. Viscoelastic relaxation: a mechanism to explain the decennial large surface displacements at the laguna del Maule silicic volcanic complex. Earth Planet. Sci. Lett. https://doi.org/10.1016/j.epsl.2019.06.005.

Okada, Y., 1992. Internal deformation due to shear and tensile faults in a half-space. Bull. Seismol. Soc. Am. 82 (2), 1018–1040.

Pedersen, R., Sigmundsson, F., Einarsson, P., 2007. Controlling factors on earthquake swarms associated with magmatic intrusions; constraints from Iceland. J. Volcanol. Geotherm. Res. 162, 73–80. https://doi.org/10.1016/j.jvolgeores.2006.12.01.

Pérez-Flores, P., Cembrano, J., Sánchez-Alfaro, P., Veloso, E., Arancibia, G., Roquer, T., 2016. Tectonics, magmatism and paleo-fluid distribution in a strike-slip setting: insights from the northern termination of the Liquiñe-Ofqui fault System, Chile. Tectonophysics. https://doi.org/10.1016/j.tecto.2016.05.016.

Perfettini, H., Avouac, J.P., 2014. The seismic cycle in the area of the 2011 Mw9.0 Tohoku-Oki earthquake. J. Geophys. Res., Solid Earth 119 (5), 4469–4515.

Perfettini, H., Avouac, J.P., Tavera, H., Kositsky, A., Nocquet, J.M., Bondoux, F., et al., 2010. Seismic and aseismic slip on the Central Peru megathrust. Nature 465 (7294), 78–81.

Pistolesi, M., Cioni, R., Bonadonna, C., Elissondo, M., Baumann, V., Bertagnini, A., Chiari, L., Gonzales, R., Rosi, M., Francalanci, L., 2015. Complex dynamics of small-moderate volcanic events: the example of the 2011 rhyolitic Cordón Caulle eruption, Chile. Bull. Volcanol. 77 (1), 1–24.

Remy, D., Froger, J.L., Perfettini, H., Bonvalot, S., Gabalda, G., Albino, F., Cayol, V., Legrand, D., De Saint Blanquat, M., 2014. Persistent uplift of the Lazufre volcanic complex (Central Andes): new insights from PCAIM inversion of InSAR time series and GPS data. Geochem. Geophys. Geosyst. 15 (9), 3591–3611.

Rosen, P.A., Gurrola, E., Sacco, G.F., Zebker, H., 2012. The InSAR scientific computing environment. In: EUSAR 2012; 9th European Conference on Synthetic Aperture Radar, pp. 730–733.

Ruz-Ginouves, J., Gerbault, M., Cembrano, J., Iturrieta, P., Leiva, F.S., Novoa, C., Hassani, R., 2021. The interplay of a fault zone and a volcanic reservoir from 3D elasto-plastic models: rheological conditions for mutual trigger based on a field case from the Andean Southern Volcanic Zone. J. Volcanol. Geotherm. Res. 107317.

Schipper, C.I., Castro, J.M., Tuffen, H., James, M.R., How, P., 2013. Shallow vent architecture during hybrid explosive-effusive activity at Cordón Caulle (Chile, 2011-12): evidence from direct observations and pyroclast textures. J. Volcanol. Geotherm. Res. https://doi.org/10.1016/j.jvolgeores.2013.06.005.

Schultz, R.A., 1996. Relative scale and the strength and deformability of rock masses. J. Struct. Geol. 18 (9), 1139–1149.

Sepúlveda, F., Lahsen, A., Dorsch, K., Palacios, C., Bender, S., 2005. Geothermal exploration in the Cordón Caulle Region, Southern Chile. In: World Geothermal Congress 2005.

Sibson, R.H., 2003. Brittle-failure controls on maximum sustainable overpressure in different tectonic regimes. AAPG Bull. 87 (6), 901–908. https://doi.org/10.1306/0129030018.

Sielfeld, G., Lange, D., Cembrano, J., 2019. Intra-Arc crustal seismicity: seismotectonic implications for the Southern Andes Volcanic Zone, Chile. Tectonics. https://doi.org/10.1029/2018TC004985.

Simpson, G., Guéguen, Y., Schneider, F., 2001. Permeability enhancement due to microcrack dilatancy in the damage regime. J. Geophys. Res. 106 (B3), 3999–4016.

Singer, B.S., Jicha, B.R., Harper, M.A., Naranjo, J.A., Lara, L.E., Moreno-Roa, H., 2008. Eruptive history, geochronology, and magmatic evolution of the Puyehue-Cordón Caulle volcanic complex, Chile. Geol. Soc. Am. Bull. 120 (5–6), 599–618.

Stanton-Yonge, A., Griffith, W.A., Cembrano, J., St. Julien, R., Iturrieta, P., 2016. Tectonic role of margin-parallel and margin-transverse faults during oblique subduction in the Southern Volcanic Zone of the Andes: insights from boundary element modeling. Tectonics 35 (9), 1990–2013.

Suppe, J., 2014. Fluid overpressures and strength of the sedimentary upper crust. J. Struct. Geol. https://doi.org/10.1016/j.jsg.2014.07.009.

Walter, T.R., Amelung, F., 2007. Volcanic eruptions following M ≥ 9 megathrust earthquakes: Implications for the Sumatra-Andaman volcanoes. Geology 35 (6), 539–542.

Wendt, A., Tassara, A., Báez, J.C., Basualto, D., Lara, L.E., García, F., 2017. Possible structural control on the 2011 eruption of Puyehue-Cordón Caulle Volcanic Complex (southern Chile) determined by InSAR, GPS and seismicity. Geophys. J. Int. https://doi.org/10.1093/gji/ggw355.

Yang, X.-M., Davis, P.M., Dieterich, J.H., 1988. Deformation from inflation of a dipping finite prolate spheroid in an elastic half-space as a model for volcanic stressing. J. Geophys. Res., Solid Earth 93 (B5), 4249–4257.

Zhan, Y., Gregg, P.M., Le Mével, H., Miller, C.A., Cardona, C., 2019. Integrating reservoir dynamics, crustal stress, and geophysical observations of the Laguna del Maule magmatic system by FEM models and data assimilation. J. Geophys. Res., Solid Earth. https://doi.org/10.1029/2019JB018681.